Self-generated Floquet modulation in a multiharmonic-dressed alignment-based magnetic-resonance system

Xu-xing Geng [1], Kai Jin [1], Wang-wang Tang,[1] Shangqing Liang,[2] Guoqing Yang,[2] Shao-ping Wu,[1] Guang-ming Huang,[1,*] and Gao-xiang Li[1,†]

[1]*Department of Physics, Huazhong Normal University, Wuhan 430079, China*
[2]*College of Electronics and Information, Hangzhou Dianzi University, Hangzhou 310018, China*

Quantum systems with multiharmonic dressing have been extensively investigated and exhibited various novel phenomena and technologies by virtue of their robust electromagnetic response. Here we mainly investigate the self-generated longitudinal Floquet modulation phenomenon of an alignment-based magnetic-resonance system with pump-probe structure dressed by two different transverse radio-frequency (rf) fields in a warm atomic cesium ensemble, both theoretically and experimentally. The self-generated Floquet modulation includes first and second harmonics, which are contributed to by linear and nonlinear processes from the weak-dressed field, respectively. The self-generated Floquet modulation dresses the alignment absorption spectra into two continua. The asymmetry of each dressed continuum is due to the generalized parity symmetry of the system being broken by the second harmonic modulation. Moreover, the nonlinear modification effect of the weak rf field on the probe verifies the existence of the four-wave mixing process in the rf band. The analytical expression, establishment process, and asymmetry analysis of the continua are given concisely. Our results can be applied to the fields of precision magnetic-field measurement, quantum control, quantum simulation, and so on. In addition, because the physical mechanism is universal, it can be applied not only to an atomic ensemble, but also to solid-state devices.

I. INTRODUCTION

The electromagnetic dressing of quantum systems is a tool for investigating quantum observables, quantum variables, and system energy [1–4]. Since the dressed field has a long-term robust effect on the system energy and the coherence establishment, quantum systems with radio frequency or microwave dressing exhibit a variety of multiphoton phenomena in various atomic vapor experiments and solid-state spin systems, including multiphoton interference process [5,6], Bloch-Siegert shifts [7,8], modifications of the Landé *g* factor [9–11], strong spin-exchange collisions [12], and so on. With the development of theory and experiments, these physical functionalities can be used in frontier fields such as magnetic resonance imaging [13], quantum computation [14], spin manipulation [15], and precision measurement [16]. Especially in the area of precision measurement, the typical application is that the intervention of the radio-frequency or microwave dressing ingeniously transforms the amplitude measurement of the physical quantity into the frequency measurement to improve the accuracy and sensitivity [17,18], which can likewise be used for absolute calibration of quantum sensors [19]. Furthermore, the spin lock formed by the coupling of the dressed field and the spin system can suppress the measurement error caused by the nonlinear Zeeman effect [20]. In

addition, Sinuco-Leon *et al.* [21,22] observed the rf multiphoton effect in the cold atom experiment, where a strong dc magnetic field and a strong rf field comodified atoms, and the existence of the rf multiphoton process reduced the sensitivity of the ground-state atomic ensemble to low-frequency noise fluctuations. Therefore, the rf multiphoton effect plays a key role in improving the signal-to-noise ratio of magnetic sensors, which is of great significance for the development of high-precision atomic magnetometers.

Periodically driven (Floquet) systems have received increasing attention in recent years. Within this area of Floquet engineering, periodic electromagnetic dressing modifies the response of the quantum system and presents numerous physical phenomena such as topological Floquet insulators [23–26], time crystal [27], prethermalization [28], Floquet Raman transition [29], and multichromatic resonance peaks [30]. Furthermore, with the continuous development of Floquet engineering, some important applications also surfaced. For example, the Floquet maser with periodically driven ^{129}Xe cell can achieve Floquet spin amplification and improve the sensitivity of the magnetic sensor to the subpicotesla level [31,32], which can be used to search for axion-like dark matter with multiple sensitive windows of particle mass [33]. Moreover, the concatenated continuous driving can flexibly control the symmetry of the quantum system [34]. In addition, quantum mixers realized by nonlinear effects in the periodically (Floquet) driven nitrogen-vacancy (NV) ensemble can be used for vector magnetic field measurements at arbitrary frequencies, with no loss of their ability to measure nanometer-scale
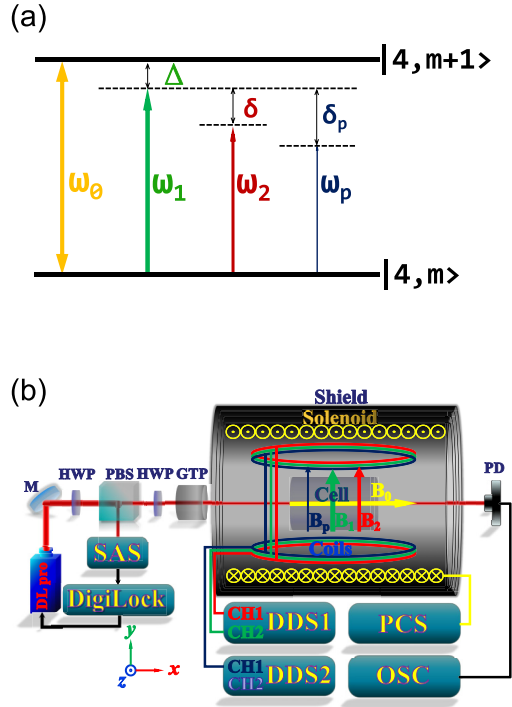
FIG. 1. (a) Two adjacent hyperfine sublevels of the ground state $F_g = 4$ of cesium atom are driven by external magnetic fields. The hyperfine structure is uniformly split with ω_0 by the offset field B_0. The two transverse rf fields $B_1(t)$ and $B_2(t)$ with frequency detuning δ modify the nondegenerate hyperfine energy levels. The modified alignment magnetic-resonance system is scanned by the probe field $B_p(t)$. (b) Experimental setup. DL pro: tunable diode laser with digital control; M: mirror; HWP: half-wave plate; PBS: polarizing beam splitter; SAS: saturated absorption spectroscopy; DigiLock: digital laser locking module; GTP: Glan-Taylor linear polarizer; Cell: Cs atomic vapor cell with antirelaxation paraffin coating; Coils: three pairs of Holmheitz coils; Shield: four-layer mumetal shield; Solenoid: low-noise nonmoment solenoid; DDS1 and DDS2: direct digital synthesized signal generators (Keysight 33500B series); PD: photodetector; PCS: precision current source (Keysight B2902A); OSC: digital storage oscilloscope (Keysight InfiniiVision DSOX6004A).

features [35]. Nevertheless, our interest is to investigate the self-generated Floquet modulation behavior of the system and the influences of this self-generated modulation on the system by dressing the alignment-based magnetic resonance system with two transverse rf fields as shown in Fig. 1(a). The research of this self-generated Floquet modulation can further reveal the physical mechanism of the interaction between the multi-modulation fields and the quantum spin system. The atomic-alignment magnetic resonance is excited by optical-radio-frequency double-resonance devices, where a linearly polarized laser is used for optical pumping and detection [36]. Moreover, the atomic alignment magnetic-resonance spectrum is a valuable topic in fundamental physics research and potential applications, which can be applied to warm atomic spin squeezing and entanglement [37–39], magnetooptical effects [40], orientation-to-alignment conversion [41], vector atomic magnetometer [42], atomic compass [43], and so on.

In this article, we concentrate on the atomic-alignment magnetic resonance dressed by two rf dressed fields [strong rf field $B_1(t)$, weak rf field $B_2(t)$], both theoretically and experimentally. This study is organized as follows. Section II gives the experimental setup of the alignment magnetic resonance dressed by two transverse rf fields and the expression of spectral detection. In Sec. III, the theoretical model of the system is presented and the physical picture of self-generated Floquet modulation is analyzed. In Sec. IV, the influences of self-generated Floquet modulation on alignment magnetic-resonance spectra are investigated experimentally. Finally, a summary for this study is given in Sec. V.

II. EXPERIMENTAL DESIGN AND ALIGNMENT-BASED MAGNETIC RESONANCE SPECTRA DETECTION

This experiment is based on the alignment magnetic resonance for ground state $F_g = 4$ in a cesium atomic ensemble with light pump-probe structure [36]. The spatial distribution and coupling schemes of magnetic fields in the experiment are shown in Fig. 1. A room-temperature glass cell for providing a paramagnetic atom sample is a homemade antirelaxation paraffin-coated cesium atom cell with a diameter of 25 mm and a length of 30 mm, which is placed in a four-layer mumetal shield isolated from the complex magnetic field environment [cf. Fig. 1(b)]. There are three processes in the experiment: prepare, interact, and probe. In the process of alignment state preparation, the tunable diode laser ($\sim$894 nm) with digital control used to prepare the alignment polarization distribution of the ground-state atoms is locked to $6\,^2S_{1/2}, F_g = 4 \leftrightarrow 6\,^2P_{1/2}, F_e = 3$ hyperfine structure by means of saturated absorption spectroscopy. To ensure that the residual circular polarization contamination in the beam is less than 1%, a Glan-Taylor linear polarizer is used to purify the polarization before entering the magnetic shield. With the condition that the relaxation of the spontaneous emission of atoms in the excited states is far greater than the laser pumping rate, the combined effect of the depopulation relaxation of the weak-field laser and the repopulation relaxation of the spontaneous emission will eventually lead to a new distribution of the ground-state atoms to establish a new dynamic balance, i.e., the atoms are aligned [44]. In the process of atom-field interaction, the hyperfine components for $F_g = 4$ are evenly split by the offset field B_0 along the light propagation direction, where the offset field B_0 is generated by a nonmoment solenoid coil driven by a low-noise precision current source. The strong-dressed field $B_1(t) = B_1 \cos \omega_1 t$ and the weak-dressed field $B_1(t) = B_2 \cos \omega_2 t$ perpendicular to the offset field B_0 are generated by two pairs of Helmholtz coils driven by two signal generators, where B_j and ω_j ($j = 1, 2$) are the amplitude and oscillating frequency, respectively. These three fields are coupled to the atoms to change the energy of the atoms and establish coherence among the sublevels, which satisfy the relationship $B_0 \gg B_1 > B_2$. In addition, the rf dressing field $B_2(t)$ is the key field for self-generated longitudinal Floquet modulation in the system. In the probe process, there are two processes: the rf probe field scanning and optical power monitoring. When the frequency ω_p of the probe field $B_p(t) = B_p \cos \omega_p t$ scans to the resonance neighborhood of the system, the rf field is coupled with the system

to establish coherence and change the population distribution, thereby partially destroying the alignment distribution established by the optical pumping process, so that atoms are forced to reabsorb light to establish a new dynamic balance. The transmitted light passing through the cell is received by the photodetector with a transimpedance amplifier and low-pass filter and recorded by the digital oscilloscope. If the dressed fields $B_1(t)$ and $B_2(t)$ are turned off, the device returns to the traditional alignment magnetic-resonance device [45]. The power variation of the pump-probe laser indirectly reflects the information of the ground-state magnetic resonance, where the relationship between the absorption of the pump-probe laser and the sublevels of the ground-state hyperfine structure can be described by Eq. (A6) in Appendix A. To gain further insight, we convert the absorption of the pump-probe laser into the form of polarization moments $C_0 m_{0,0}^{\text{lab}} + C_2 m_{2,0}^{\text{lab}}$, where the atomic multipole moments $m_{0,0}^{\text{lab}}$ and $m_{2,0}^{\text{lab}}$ are the monopole moment and alignment [36], respectively. The coefficients C_0 and C_2 are related to the analyzing power, amplifier gain factor, optical power, and so on. Since $m_{0,0}^{\text{lab}} = 1/3$ is a number related to the population of atoms and has nothing to do with the information carried by the spectra, the alignment magnetic-resonance spectra can be simplified to

$$S^{\text{lab}}(\omega_p) = C_2 m_{2,0}^{\text{lab}}. \tag{1}$$

Details on the laser-detected alignment magnetic-resonance spectra are given in Appendix A.

III. THEORETICAL MODEL ESTABLISHMENT AND ANALYSIS

To investigate the double-dressed alignment magnetic-resonance spectra, the quantization axis z is selected in the direction of the offset field B_0. In this original representation of the calculation, the atom sees the total magnetic field $\hat{B}_{\text{tot}} = B_0 \hat{e}_z + [B_1(t) + B_2(t) + B_p(t)]\hat{e}_x$. The Hamiltonian H_{tot} of the magnetic fields interacting with atom is given by $H_B = -\hat{\mu} \cdot \hat{B}_{\text{tot}} = g_F \mu_B \sum_{i=-1}^{i=1} F_i B^i$ [46,47], where the physical constants g_F and μ_B, the angular momentum F_i, and the magnetic-field component B^i are the hyperfine-structure Landé g factor, the Bohr magneton, the hyperfine angular momentum in covariant spherical harmonic representation, and the magnetic-field component in the contravariant spherical harmonic representation, respectively. The covariant spherical harmonic representation components e_j (with $j = 0, \pm 1$) in the Cartesian coordinate representation are given by $e_{\pm 1} = \mp \frac{1}{\sqrt{2}}(e_x \pm ie_y), e_0 = e_z$. Additionally, the contravariant spherical harmonic representation components e^j (where $j = 0, \pm 1$) in the Cartesian coordinate representation are defined by the relations $e^{\pm 1} = \mp \frac{1}{\sqrt{2}}(e_x \mp ie_y), e^0 = e_z$ [48]. In the spherical harmonic representation, when the rotating-wave approximation condition is satisfied, by going into the rotating frame with frequency ω_1 and neglecting the counterrotating terms, the Hamiltonian for the system in the spherical harmonic representation is given by

$$H_{\text{tot}} = H_0 + H_1 + H_2 + H_p, \tag{2}$$

with

$$H_0 = \Delta F_0, \tag{3a}$$

$$H_1 = \Omega_1(F_{-1} - F_1), \tag{3b}$$

$$H_2 = \Omega_2\big(F_{-1}e^{i\delta t} - F_1 e^{-i\delta t}\big), \tag{3c}$$

$$H_p = \Omega_p\big(F_{-1}e^{i\delta_p t} - F_1 e^{-i\delta_p t}\big), \tag{3d}$$

where detuning $\Delta = \omega_0 - \omega_1$ is the detuning of the Larmor precession frequency $\omega_0 = \mu_B g_F B_0$ generated by the offset field B_0 and the frequency ω_1 of the strong rf field $B_1(t)$. The detunings δ and δ_p are given by $\delta = \omega_2 - \omega_1$ and $\delta_p = \omega_p - \omega_1$. The Rabi frequencies of the strong rf field, the weak rf field, and the probe field are defined by $\Omega_j = \mu_B g_F B_j / 2\sqrt{2}$ (with $j = 1, 2, p$). The spherical components F_μ of the hyperfine angular momentum can be expressed in terms of the basis $\{|4, m\rangle\}$ as $F_\mu = 2\sqrt{5} \sum_{m=-4}^{m=4} C_{4m1\mu}^{4\mu+m} |4, m+\mu\rangle\langle 4, m|$ with $\mu = 0, \pm 1$, where the coefficient $C_{\diamond\diamond\diamond\diamond}^{\diamond\diamond}$ is the Clebsch-Gordan coefficient and the operator $|4, m+\mu\rangle\langle 4, m|$ represents the transition from $|4, m\rangle$ to $|4, m+\mu\rangle$ [48].

It is convenient to further pursue an analytical method for physical insights. This can be achieved by imposing the following conditions. (i) The Zeeman splitting ω_0 of the longitudinal offset field B_0 and the Rabi frequencies ω_1 and ω_2 of the two transverse rf fields satisfy the relation $\omega_0 \gg \Omega_1 > \Omega_2$. On the one hand, this condition ensures that the possible presence of longitudinal components for the rf fields $B_1(t)$ and $B_2(t)$ in the direction of the offset field B_0 due to the fact that both rf fields $B_1(t)$ and $B_2(t)$ are not strictly orthogonal to the offset field B_0 can be ignored by the rotating-wave approximation during the experiment. On the other hand, it is ensured that the Hamiltonian of the offset field B_0 and the strong rf field $B_1(t)$ satisfies the diagonalization condition, and the Hamiltonian of the weak rf field $B_2(t)$ satisfies the perturbation condition. (ii) The Rabi frequency Ω_p of the probe field is much smaller than the Rabi frequency Ω_2 of the rf field $B_2(t)$, i.e., $\Omega_2 \gg \Omega_p$, so the influence of the probe field on the system can be ignored. (iii) The detuning δ of the two rf dressed fields is smaller than the linewidth Γ of the system, i.e., $\delta < \Gamma$. All parameters are experimentally manageable. Typical values of the optimized experimental parameters are $\omega_0 \approx 152.210$ kHz, $\omega_1 \approx 152.210$ kHz, $\omega_2 \approx 152.220$ kHz, $\Omega_1 \approx 810$ Hz, $\Omega_2 \approx 243$ Hz, $\Gamma \approx 50$ Hz, and $\Omega_p \approx 20$ Hz, which satisfy the above constraints. All parameters are tuned in the neighborhood of these typical values during the experiment.

To gain further insight, the Hamiltonian $H_0 + H_1$ is diagonalized into the dressed-state $|4, m'\rangle$ representation, where the eigenvalue is $\lambda = m'\Omega$ $(m' = -4, \ldots, 4)$ with $\Omega = \sqrt{\Delta^2 + 2\Omega_1^2}$. The eigenvector is given by $|4, m'\rangle = \sum_m |4, m\rangle D_{mm'}^{(4)*}(0, \beta, 0)$ and the Euler angle β satisfies $\cos\frac{\beta}{2} = \sqrt{\frac{\Omega+\Delta}{2\Omega}}$ and $\sin\frac{\beta}{2} = \sqrt{\frac{\Omega-\Delta}{2\Omega}}$, in which the rotation transformation $D_{mm'}^{(k)}(\psi, \theta, \phi)$ is the Wigner D functions defined by analytic continuation with the Euler angles ψ, θ, and ϕ [49]. The hyperfine angular momentum operator F_j' can be expanded into $F_\nu' = 2\sqrt{5} \sum_{m'=-4}^{m'=4} C_{4m'1\nu}^{4m'+\nu} |4, m'+\nu\rangle\langle 4, m'|$ with $\nu = 0 \pm 1$ in the dressed-state representation, where

the operator $|4, m' + \nu\rangle\langle 4, m'|$ represents the transition from $|4, m'\rangle$ to $|4, m' + \nu\rangle$. The angular momentum operators between the two representations satisfy $F_q = \sum_{q'} F'_{q'} D^{(1)}_{q'q}(0, \beta, 0)$ with $q, q' = 0, \pm 1$. Next, the Hamiltonian H_2 of the weak rf field $B_2(t)$ and the Hamiltonian H_p of the probe field $B_p(t)$ enter the dressed-state representation. According to the effective Hamiltonian theory [50], the Hamiltonian is perturbed to the second order. Therefore, the effective Hamiltonian $H'(t)$ of the system in the dressed-state representation is

$$H'(t) = H_s^d(t) + H_p^d(t), \qquad (4)$$

with

$$H_s^d(t) = \Omega_2 m(t) F'_0, \qquad (5a)$$

$$H_p^d(t) = \Omega_p [f_\pm(t) F'_{-1} e^{-i\delta_\pm t} - f_\pm^*(t) F'_1 e^{i\delta_\pm t}], \qquad (5b)$$

$$m(t) = 2\sqrt{2} \cos\frac{\beta}{2} \sin\frac{\beta}{2} \cos\delta t$$
$$- 2\frac{\Omega_2}{\Omega} \cos^2\frac{\beta}{2} \sin^2\frac{\beta}{2} \cos 2\delta t, \qquad (5c)$$

$$f_\pm(t) = \frac{1 \pm \cos\beta}{2} + \sqrt{2}\frac{\Omega_2}{\Omega + \delta} \cos\frac{\beta}{2} \sin^3\frac{\beta}{2} e^{-i\delta t}$$
$$- \sqrt{2}\frac{\Omega_2}{\Omega - \delta} \cos^3\frac{\beta}{2} \sin\frac{\beta}{2} e^{i\delta t}, \qquad (5d)$$

where $H_s^d(t)$ and $H_p^d(t)$ are the system Hamiltonian and the probe Hamiltonian in the dressed-state representation, respectively. The dimensionless parameters $m(t)$ and $f_\pm(t)$ are the self-generated Floquet modulation coefficient and the modified probe coefficient, respectively (see Appendix B for details). The detuning $\delta_\pm$ and frequency shift ω_{BS} are given by $\delta_\pm = \Omega + \omega_{\text{BS}} \mp \delta_p$ and $\omega_{\text{BS}} = \Omega_2^2(\frac{\sin^4\frac{\beta}{2}}{\Omega + \delta} + \frac{\cos^4\frac{\beta}{2}}{\Omega - \delta})$, respectively. The subscript "+" ("−") corresponds to the right (left) sideband of the spectra.

In the double-dressed system, the Hamiltonian (5a) and Fig. 2(a) show that the strong-dressed field $B_1(t)$ splits each atomic energy level equidistantly with energy Ω in the dressed-state representation. The weak rf field $B_2(t)$ has nonresonant one-photon and two-photon modifications to the system. For nonresonant one-photon modification, the dressed atoms absorb the π photons from the dressed field $B_2(t)$ in different transition channels to synthesize Floquet first-harmonic modulation $2\sqrt{2}\Omega_2 \cos\frac{\beta}{2} \sin\frac{\beta}{2} \cos\delta t$ [cf. transition 1 in Fig. 2(a)]. For nonresonant two-photon modification, the weak rf field $B_2(t)$ makes the system produce time-dependent second harmonic modulation and time-independent energy-level shifting effects. On the one hand, the dressed atoms undergo nonresonant cascaded two-photon transitions in two adjacent two-photon transition channels, wherein the dressed atoms simultaneously absorb two nonresonant σ rf photons from the dressed field $B_2(t)$ in each channel, so that these two cascaded two-photon processes jointly synthesize the Floquet second-harmonic modulation $-2\frac{\Omega_2^2}{\Omega} \cos^2\frac{\beta}{2} \sin^2\frac{\beta}{2} \cos 2\delta t$; see transition 2 in Fig. 2(a). On the other hand, the dressed atoms undergo nonresonant Raman transitions in two adjacent two-photon transition channels, wherein the dressed atoms absorb and emit two nonresonant σ rf photons from the dressed field
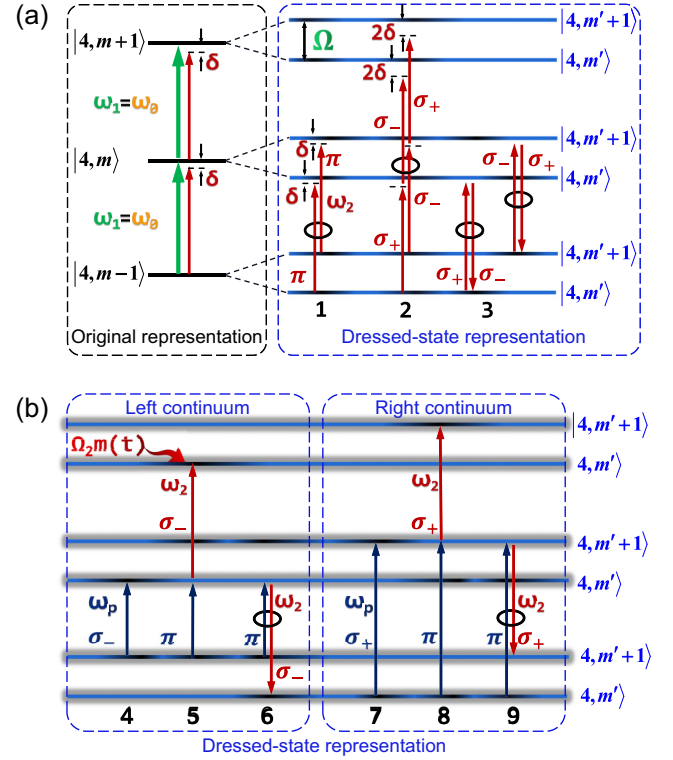

FIG. 2. Hyperfine energy-level structure of doubly dressed magnetic resonance. (a) System dressed by two transverse rf fields. In the original representation with the basis $\{|4, m\rangle\}$, the nine hyperfine sublevels are uniformly split by the offset field B_0 and their frequency interval is ω_0 (for brevity only three adjacent sublevels are given). The frequency ω_1 of the strong dressed field $B_1(t)$ is resonant with the frequency ω_0 and detuned from the weak rf field $B_2(t)$. Each hyperfine sublevel in the original representation is uniformly dressed by strong rf field $B_1(t)$ into nine new sublevels in the dressed-state representation (for brevity only two adjacent sublevels are given in the dressed-state representation). In the dressed-state representation with the basis $\{|4, m'\rangle\}$, the dressed field $B_2(t)$ modifies the energy levels of the system. Transition 1: The nonresonant process of two single rf photons generates first harmonic modulation. Transition 2: Two cascade two-photon processes generate second harmonic modulation. Transitions 1 and 2 constitute the Floquet modulation $\Omega_2 m(t)$. Transition 3: Two Raman two-rf-photon processes produce ω_{BS}. (b) The dressed field $B_2(t)$ modifies the rf probe process. Transition 4 (7): Single-photon process in the left (right) continuum. Transition 5 (8): The cascade four-wave mixing modification in the left (right) continuum. Transition 6 (9): Raman four-wave mixing modification in the left (right) continuum.

$B_2(t)$ in each channel, so that the two Raman two-photon processes jointly produce a Bloch-Siegert-like shift ω_{BS} [8]; see transition 3 in Fig. 2(a). Therefore, due to the presence of the dressed field $B_2(t)$, the system will automatically generate the Floquet modulation $\Omega_2 m(t)$.

In the probe process, because the probe is modified by the weak rf field $B_2(t)$, there is not only the linear absorption process, but also the obvious nonlinear absorption process; see Fig. 2(b) and Hamiltonian (5b). Taking the right sideband as an example, for the linear absorption process, the atom absorbs a rf photon with frequency $\omega_p = \omega_1 + \Omega + \omega_{\text{BS}}$ in

the probe field $B_p(t)$ and cause $\Delta m' = 1$ transition with the coupling strength $\frac{1+\cos\beta}{2}\Omega_p$; see transition 7 in Fig. 2(b). For nonlinear absorption processes, there are two channels of Raman and cascade four-wave mixing [51,52]. In the cascade four-wave mixing process, the dressed atoms absorb one rf photon with frequency ω_p and one rf photon with frequency ω_2 in the probe field $B_p(t)$ and dressed field $B_2(t)$, respectively, while the dressed field $B_1(t)$ emits two rf photons with frequency ω_1, in which the frequencies satisfy the relation $\Omega + \omega_{BS} - \delta - \delta_p \approx 0$ in the entire process; see transition 8 in Fig. 2(b). In the Raman four-wave mixing process, the dressed atoms absorb a rf photon of frequency ω_p in the probe field $B_p(t)$ and then emit a rf photon of frequency ω_2 into the dressed field $B_2(t)$, while the dressed field $B_1(t)$ emits a rf photon with frequency ω_1 and absorbs the photon with frequency ω_1, where these frequencies satisfy the relation $\Omega + \omega_{BS} - \delta + \delta_p \approx 0$ in the entire process; see transition 9 in Fig. 2(b). All of these transitions partially change the

atomic alignment distribution established by optical pumping. Eventually, the atoms are forced to continuously absorb laser photons and establish new dynamic alignment distribution.

To find the transparent form of dressed spectra (1), the Hamiltonian (4) with Floquet transformation is brought into the evolution equation, where the evolution of the polarized atomic ensembles governed by the master equation $\dot{\rho}(t) = -i[H', \rho(t)] + L\rho(t)$; see Appendix B for details of the derivation. The density matrix $\rho(t)$ is straightforwardly expanded to $\rho(t) = \sum_{k=0}^{k=2F} \sum_{q=-k}^{q=k} m_{k,q}(t) T_{k,q}$ with a set of kth-order irreducible tensor bases $\{T_{k,q}\}$ [49] and brought into the master equation, so that the expression of the steady-state alignment transmission spectra is analytically given by

$$S^{\text{lab}}(\omega_p) = S_-^{\text{lab}}(\omega_p) + S_+^{\text{lab}}(\omega_p), \qquad (6)$$

with

$$S_\pm^{\text{lab}}(\omega_p) = C\left\{\frac{1}{3} - \frac{1}{4}\sum_{l=-\infty}^{l=+\infty}\left[\frac{\left|\Omega_\pm^{(l)}\right|^2}{\Delta_\pm^{(l)2}+\gamma_{1\pm}^2} - \frac{3\left|\Omega_\pm^{(l)}\right|^4}{4^2\left(\Delta_\pm^{(l)2}+\gamma_{1\pm}^2\right)\left(\Delta_\pm^{(l)2}+\gamma_{2\pm}^2\right)}\right]\right\}, \qquad (7)$$

where the detuning $\Delta_\pm^{(l)} = l\delta + \delta_\pm$, the coefficient $C = 3C_2 D_{0,0}^{(2)*}(0, \frac{\pi}{2}, \frac{\pi}{2}) D_{0,0}^{(2)*}(0, \beta, 0) m_{0,0}^{\text{lab}}$, and the spectral linewidths $\gamma_{1\pm}^2 = \Gamma^2 + |\Omega_\pm^{(l)}|^2/4$ and $\gamma_{2\pm}^2 = (\Gamma^2 + |\Omega_\pm^{(l)}|^2)/4$. The linewidth Γ is the equivalent relaxation rate of the alignment. Spectra $S_-^{\text{lab}}(\omega_p)$ and $S_+^{\text{lab}}(\omega_p)$ correspond to the left continuum and the right continuum, respectively. Details of the derivation of Eq. (6) can be found in Appendix B. The Rabi frequency with second-order correction is given by

$$\begin{aligned}
\Omega_\pm^{(l)} =&\ \frac{1 \pm \cos\beta}{2}\Omega_p \sum_{n=-\infty}^{n=+\infty} J_{2n+l}(\xi_1)J_n(\xi_2) \\
&- \cos^3\frac{\beta}{2}\sin\frac{\beta}{2}\frac{\sqrt{2}\Omega_2\Omega_p}{\Omega-\delta}\sum_{n=-\infty}^{n=+\infty} J_{2n+l+1}(\xi_1)J_n(\xi_2) \\
&+ \cos\frac{\beta}{2}\sin^3\frac{\beta}{2}\frac{\sqrt{2}\Omega_2\Omega_p}{\Omega+\delta}\sum_{n=-\infty}^{n=+\infty} J_{2n+l-1}(\xi_1)J_n(\xi_2),
\end{aligned}$$
$$(8)$$

with arguments $\xi_1 = \cos\frac{\beta}{2}\sin\frac{\beta}{2}\frac{2\sqrt{2}\Omega_2}{\delta}$ and $\xi_2 = \cos^2\frac{\beta}{2}\sin^2\frac{\beta}{2}\frac{\Omega_2^2}{\Omega\delta}$, where function $J_n(z)$ is the Bessel function of the first kind [53]. The arguments ξ_1 and ξ_2 are respectively derived from the first harmonic and the second harmonic in the self-generated Floquet modulation. From the spectra (6) and the Rabi frequency (8), it can be seen that if the condition $\xi_2 \to 0$ is satisfied, only the first harmonic in the self-generated Floquet modulation $\Omega_2 m(t)$ is considered, and the equivalent Rabi frequency $\Omega_\pm^{(l)}$ returns to $\Omega_\pm^{(l)} = \frac{1\pm\cos\beta}{2}\Omega_p J_l(\xi_1)$. When the system satisfies the resonance condition $\delta_\pm = 0$, it is found that the Hamiltonian (4) satisfies the generalized parity symmetry, that is, $PH'(t + T/2)P = H'(t)$, where the definition of the generalized parity operator P is the energy reversal

$(F_0 \to -F_0)$ of the system after half a period of modulation $(t \to t + T/2)$ [54]. The continuum is symmetrical as shown by the hollow green circles in Fig. 3(a), which is similar to the resonance fluorescence spectrum with one modulated laser light discussed previously [55,56]. Essentially, symmetry for continuum is due to the fact that the Hamiltonian modulated by the first harmonic satisfies generalized parity symmetry [57]. Furthermore, only considering the nonlinear modification of the probe by the field $B_2(t)$, the two types of four-wave mixing process symmetrically modify the profile of the continuum to make the profile lighter [cf. the solid blue circles in Fig. 3(a)]. However, notwithstanding that only considering the first term of the Rabi frequency $\Omega_\pm^{(l)}$, the continuum is pronouncedly asymmetric; see the hollow black circles in Fig. 3(b). The relative magnitude of the extremum amplitudes of each continuum depends on the second harmonic modulation parameter ξ_2 and on the relative magnitude of the extremums of the square of the absolute value of the probe Rabi frequency $|\Omega_\pm^{(l)}|^2$; see Appendix C for more details about $|\Omega_\pm^{(l)}|^2$. The reason for the asymmetry of the continuum, from the perspective of symmetry, is that the second harmonic modulation breaks the symmetry of the system. Therefore, the self-generated Floquet modulation $\Omega_2 m(t)$ modifies the symmetry and profile of the alignment magnetic resonance spectra and the generalized parity of the Hamiltonian with this Floquet modulation is absent [54] [the solid purple circles in Fig. 3(b)].

IV. EXPERIMENTAL AND THEORETICAL VERIFICATION

Experimentally, the system is scanned by a low-intensity transverse rf field $B_p(t)$, and the magnetic-resonance alignment magnetic-resonance spectra $S^{\text{lab}}(\omega_p)$ can be observed by
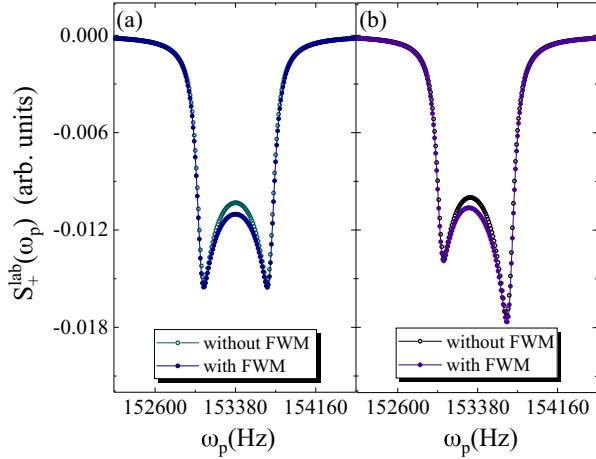
FIG. 3. The right continua of alignment magnetic-resonance spectra $S^{\text{lab}}(\omega_p)$ with doubly dressed fields corresponding to the different modifications from dressed field $B_2(t)$. (a) Hollow green circles: The system is modulated by the self-generated first harmonic and the probe is not modified by the four-wave mixing process. Solid blue circles: The system is modulated by the self-generated first harmonic and the probe is modified by the four-wave mixing process. (b) Hollow black circles: The system is modulated by the self-generated first and second harmonics and the probe is not modified by the four-wave mixing process. Solid purple circles: The system is modulated by the self-generated first and second harmonics and the detection is modified by the four-wave mixing process. The parameters used in the calculation are $\omega_0 = 152.210$ kHz, $\omega_1 = 152.210$ kHz, $\omega_2 = 152.220$ kHz, $\Omega_1 = 810$ Hz, $\Omega_2 = 243$ Hz, and $\Omega_p = 20$ Hz.

FIG. 4. The alignment magnetic-resonance spectra $S^{\text{lab}}(\omega_p)$ with double rf dressing fields. The black circles are the experimental data and the blue continuous line is the theoretical fit. (a) The alignment magnetic resonance spectra are dressed by a strong rf field $B_1(t)$ with resonant frequency $\omega_1 = \omega_0 = 152.210$ kHz. (b) The alignment magnetic-resonance spectra are dressed by two rf fields $B_1(t)$ and $B_2(t)$, where the strong one resonates with frequency ω_0 and the weak one is detuned at 10 Hz ($\omega_2 = \omega_1 + 10$ Hz). (c) The alignment magnetic-resonance spectra are dressed by two nonresonant rf fields $B_1(t)$ and $B_2(t)$ with $\omega_1 = 152.310$ kHz and $\omega_2 = 152.320$ kHz. Other parameters are $\Omega_1 \approx 810$ Hz, $\Omega_2 \approx 162$ Hz, $\Omega_p \approx 20$ Hz, and $\Gamma \approx 50$ Hz.

monitoring changes in the optical power of the probe light. For the system dressed by a intense rf field $B_1(t)$, the alignment magnetic-resonance spectra show the standard Autler-Townes splittings as shown in Fig. 4(a), where the frequency separation between the two splittings depends on the Rabi frequency Ω_1 and the detuning Δ. However, for the system dressed by two rf fields $B_1(t)$ and $B_2(t)$, when the frequency ω_1 of the strong dressed field $B_1(t)$ is set to resonate with the Larmor frequency ω_0 and the frequency ω_2 is detuned with ω_1 by 10 Hz, compared with the Autler-Townes absorption spectra produced by one dressed field [17,58], the presence of the weak dressed field $B_2(t)$ leads to the pronouncedly asymmetric continuous broadened modification of the sidebands for the alignment magnetic-resonance spectra; see Fig. 4(b). The center of the broadened sideband continuum is located at $\omega_1 \pm (\Omega + \omega_{\text{BS}})$. With the condition of the weak probe, each sideband continuum is the accumulation of infinite Lorentz functions whose center is $\omega_1 \pm (\Omega + \omega_{\text{BS}} + l\delta)$, linewidth is $\gamma_{1\pm}$, and weight factor is $|\Omega_{\pm}^{(l)}|^2$ with the modification from rf field $B_2(t)$. There are two inflection points in the edge area of each asymmetric continuum, and the frequencies $\zeta_{\pm 2}$ and $\zeta_{\pm 1}$ correspond to the frequency positions for maxima and submaxima, respectively. The sideband continua quickly decrease to zero after the maxima. The experimental data (black circles) match well with the theoretical predictions (blue continuous line). The physical picture for the formation of the spectra can be explained concisely as follows: the alignment magnetic-resonance spectrum without dressing from rf field $B_2(t)$ is split into an Autler-Townes doublet by
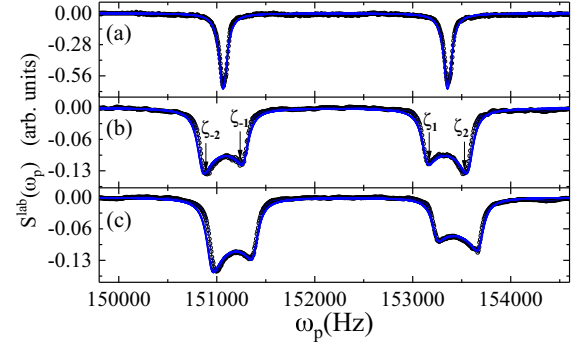
the transverse strong rf field $B_1(t)$. Next, the self-generated Floquet modulation modulates the sidebands of the Autler-Townes splittings into asymmetrical continua. Note that the asymmetry of the continuum originates from the second harmonic modification in the self-generated Floquet modulation. Moreover, when the strong dressed field $B_1(t)$ is detuned to the Larmor precession frequency ω_0, the left and right continua are recognizably asymmetrical as shown in Fig. 4(c). The physical mechanism is that the Rabi frequencies $\Omega_{\pm}^{(l)}$ of the left and right continua are not equal due to detuning, i.e., $\beta \neq \pi/2$. The self-generated Floquet modulation field and the four-wave mixing processes make different modifications to the two continua. From the perspective of parity symmetry, due to the appearance of the detuning $\Delta \neq 0$, the generalized parity of the system is completely destroyed. Furthermore, the frequency detuning δ of the two dressed fields affects the magnitude of the maxima and submaxima of the continua of the alignment magnetic-resonance spectra. Figure 5 shows the right continua of alignment magnetic-resonance spectra for different detuning δ. It is obvious that the continuum with a detuning of 10 Hz between the two dressed fields is more symmetrical than the continuum with a detuning of 5 Hz. The physical mechanism can be revealed as follows: the asymmetric modification of the spectral continuum originates from the second harmonic in the self-generated Floquet modulation. The detuning δ affects the magnitudes of the arguments ξ_1 and xi_2 of the Bessel functions $J_l(\xi_1)$ and $J_n(\xi_2)$ of the first kind in the probe Rabi frequency (8). when the detuning δ increases, the argument ξ_2 of the Bessel function $J_n(\xi_2)$ decreases, and the corresponding value decreases, so the influence of the second harmonic modulation on the asymmetry of the continuum decreases. According to Appendix C, it can be approximated that the relative magnitudes of the maxima and submaxima for the spectral sideband continuum depend
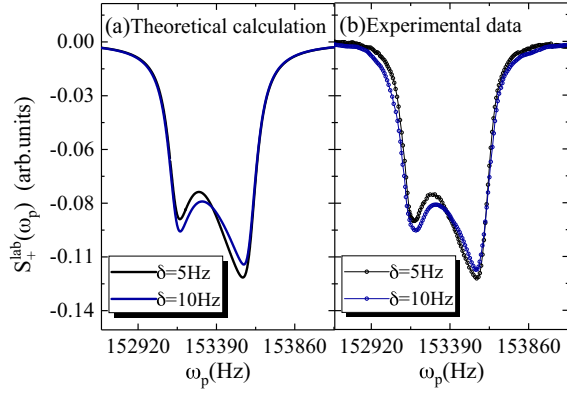
FIG. 5. The right continua of alignment magnetic-resonance spectra $S^{\text{lab}}_+(\omega_p)$ with different detuning δ of two rf dressed fields. (a) Theoretical analytical calculation: The black and blue solid lines correspond to detuning at 5 Hz and 10 Hz, respectively. (b) Experimental measurement data: The hollow black and blue circles correspond to detuning of 5 Hz and 10 Hz, respectively. The parameters are $\omega_0 = 152.210$ kHz, $\omega_1 = 152.210$ kHz, $\Omega_1 \approx 810$ Hz, $\Omega_2 \approx 162$ Hz, and $\Omega_p \approx 20$ Hz.

on the ratio of the maxima and submaxima of the square of the absolute value of the probe Rabi frequency. Under the limiting condition that the argument ξ_2 tends to zero, the continuum is symmetric, which is similar to the symmetric continua phenomenon previously seen in quantum dots [59] and in the negatively charged single silicon vacancy (V^-_{Si}) color centers in 4H silicon carbide (4H-SiC) [56].

It can be captured from Fig. 6 that, when the Rabi frequency Ω_1 increases within a certain range, the frequencies ζ_1 and ζ_2 corresponding to the two extreme values for the right continuum increase linearly, while the frequencies ζ_{-1} and ζ_{-2} corresponding to the two extreme values of the left continuum decrease linearly. This change in linear behavior is similar to that of the two splittings in the Autler-Townes spectra [60], both of which are caused by the strong dressed field $B_1(t)$.
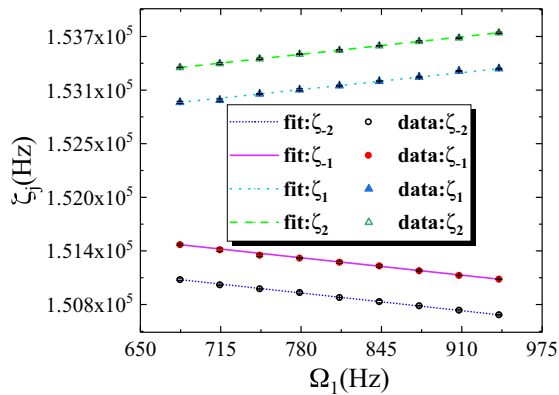

FIG. 6. The four extreme positions ζ_j ($j = \pm1, \pm2$) of the alignment magnetic-resonance spectra versus the Rabi frequency Ω_1 of the strong dressed field $B_1(t)$, in which subscript j takes $1(-1)$ and $2(-2)$ to correspond to the positions of the submaxima and maxima of the right (left) continuum for the alignment magnetic resonance spectrum, respectively. The parameters are $\omega_0 = 152.210$ kHz, $\omega_1 = 152.210$ kHz, $\omega_2 = 152.220$ kHz, $\Omega_2 \approx 162$ Hz, and $\Omega_p \approx 20$ Hz.
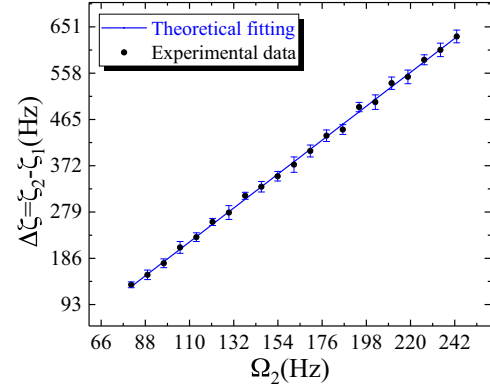

FIG. 7. The positional interval $\Delta\zeta = \zeta_2 - \zeta_1$ between the maxima and submaxima of the right continuum for the alignment magnetic-resonance spectra versus the Rabi frequency Ω_2 of the weak field $B_2(t)$. The parameters used in the calculation and experiment are $\omega_0 = 152.210$ kHz, $\omega_1 = 152.210$ kHz, $\omega_2 = 152.220$ kHz, $\Omega_1 \approx 810$ Hz, and $\Omega_p \approx 20$ Hz.

Moreover, the frequency interval $\Delta\zeta = |\zeta_{\pm2} - \zeta_{\pm1}|$ of the extreme values in each continuum remains constant during the change of the strong dressed field $B_1(t)$. The reason why the frequency interval $\Delta\zeta$ remains the same is that the argument ξ_1 of Bessel function $J_l(\xi_1)$, which mainly determines the extreme positions, is unchanged. Furthermore, under the condition that the Rabi frequency Ω_1 of the strong rf field $B_1(t)$ remains constant and the Rabi frequency Ω_2 of the weak rf field $B_2(t)$ changes in a certain small range, the frequency interval $\Delta\zeta$ between the maxima and submaxima of the right continuum of the alignment magnetic-resonance spectrum can be approximately considered to vary linearly with the Rabi frequency Ω_2; see Fig. 7. it is noteworthy that the approximately linear curve does not extrapolate to zero at $\Omega_2 = 0$. This phenomenon is revealed as follows: on the one hand, the extreme positions ζ_j ($j = \pm1, \pm2$) of the spectral continuum is related to the extreme positions of the square $|\Omega^{(l)}_{\pm}|^2$ of the absolute value of the probe Rabi frequency. The positions $\mathcal{P}_{\text{right}}$ and $\mathcal{P}_{\text{left}}$ of the maxima and submaxima of $|\Omega^{(l)}_{\pm}|^2$ in the right continuum for the alignment magnetic resonance spectra are approximately $\mathcal{P}_{\text{right}} = [\xi_1] - k_2$ and $\mathcal{P}_{\text{left}} = -|[\xi_1] + k_1|$ with (k_1 or $k_2 = 0, 1, 2, \ldots$), where $[x]$ denotes the integer part satisfying the relation $[x] \leqslant x < [x] + 1$. When the argument ξ_2 is large, k_1 and k_2 are not equal. the interval $\Delta\mathcal{P}$ between the maxima and submaxima is $\Delta\mathcal{P} = |2[\xi_1] + k_1 - k_2|$. Then in this case, when Ω_2 directly tends to 0, argument ξ_1 tends to 0, but $\Delta\mathcal{P}$ is $|k_1 - k_2| \neq 0$. On the other hand, because the spectral continuum is synthesized by the summation of infinite Lorentzian peaks with different resonance points, the average effect of the summation is also considered. In addition, because the magnitude of the value of $|\Omega^{(l)}_{\pm}|^2$ corresponding to the different l on both sides of the extreme of $|\Omega^{(l)}_{\pm}|^2$ is not symmetrical with respect to the extreme position, the average effect of the summation will also shift the extreme position of the continuum. According to the analysis of the above two aspects, the approximately linear curve of Fig. 7 does not extrapolate to zero within the range of our typical

experimental parameters. Considering the results of Figs. 6 and 7 comprehensively, the Rabi frequency Ω_1 or Ω_2 of the dressed field $B_1(t)$ or $B_2(t)$ corresponds to the frequency ζ_j corresponding to the extreme values in the continua in a linear one-to-one correspondence. This linear conversion relationship between frequency and amplitude has certain reference significance in the field of precision measurement of magnetic fields [18]. Moreover, two rf fields with small frequency detuning δ can be measured simultaneously for our system.

V. CONCLUSION

We investigate an alignment magnetic-resonance system dressed by two transverse rf fields with different frequencies, both theoretically and experimentally. The alignment magnetic resonance spectra differ qualitatively from both the one dressing case [60,61] and the two dressing case with two fields of equal frequencies [59,62]. Due to the dressing from the weak field $B_2(t)$, the system self-generates robust longitudinal Floquet modulation $\Omega_2 m(t)$ with first and second harmonics. The modulation of the self-generated first harmonic to the system changes the Autler-Townes doublet structure into a double symmetric continua, where the generalized parity of the system is present. The two continua are composed of infinite Lorentz spectra accumulated and separated by the Rabi frequency Ω_1 of the strong dressed field; the bandwidth of each continuum is determined by the Rabi frequency Ω_2 of the weak dressed field. However, the self-generated second harmonic modulation changes the continua from symmetric to asymmetric because the modulation destroys the generalized parity symmetry of the system. Moreover, the nonlinear modification of the probe by the weak rf field $B_2(t)$ also verifies the existence of four-wave mixing in the radio frequency band. Furthermore, the frequency corresponding to the extreme points of the continua has the linear one-to-one correspondence with the Rabi frequency of the modified field, which is a constructive guide to the study of indirect measurement of physical quantities.

In addition, our results also show that the ground-state atoms of the coated alkali-metal atom gas cell have the advantages of narrow linewidth and high stability, which can be used as a supplementary platform for studying the interaction between electromagnetic fields and atoms in the radio frequency band. The direct application of the alignment magnetic-resonance system modified by double harmonics is the precise measurement for rf magnetic fields [63,64]. Since this double-dressing structure can change the profile of the spectra and control the spectral width, it can be used for spectral shaping [65,66]. It can also be used for the research and development of tunable wideband rf sources and receivers [67,68]. In addition, the spectra can also be used to study atomic optical filters [69,70]. Therefore, the magnetic dressing provides a versatile tool for studying dressed spectra [71], precision measurements [17], quantum control [72,73], quantum simulations [74], and so on.

APPENDIX A: DERIVATION OF LASER-DETECTED ALIGNMENT-BASED MAGNETIC-RESONANCE SPECTRA (1)

In the experiments, alignment magnetic-resonance spectra are obtained with a weakly resonant linearly polarized light pump-probe structure [75], where the resonant linearly polarized light is used to prepare the ground-state atomic-alignment polarization state on the one hand, and to detect the ground-state magnetic-resonance spectra on the other hand. The detailed process is that weak resonant linearly polarized laser aligns with the hyperfine structure transition $6\,^2S_{1/2}$, $F_g = 4 \iff 6\,^2P_{1/2}$, $F_e = 3$. Weak lasers pump atoms from the ground-state hyperfine sublevels to the excited hyperfine sublevels, where a depopulation process occurs. Since the pumping rate is much smaller than the spontaneous emission rate, the spontaneous emission of the excited state brings the atoms back to the ground-state hyperfine sublevels for a repopulation process. When the system reaches a steady state, the depopulation process of the laser and the repopulation process of the spontaneous emission make the atoms at the hyperfine sublevels establish a dynamic equilibrium [76]; at the same time, the distribution of thermal atoms also changes from the thermal equilibrium distribution [77] to the alignment polarization distribution [78]. When the polarized atoms undergo magnetic-resonance interaction with the magnetic fields, the alignment distribution will be partially destroyed, and the atoms are forced to absorb laser photons to establish a new dynamic equilibrium. During this process, the transmitted optical power of the probe laser will change, and this change can reflect the atomic-alignment magnetic resonance information. Next, we obtain the probe expressions of the alignment magnetic-resonance spectra by means of the master equation [79,80]. In the laboratory frame, the quantization axis z is set as the polarization direction of the pump-probe laser and the atoms are coupled with the laser in the configuration of the π transition. The master equation for the interaction between the resonant linearly polarized pump-probe laser and atoms and spontaneous emission relaxation process is

$$\frac{d\rho}{dt} = -i[\mathcal{H}_{\text{laser}}, \rho] + \mathcal{L}_{\text{se}}\rho, \tag{A1}$$

with

$$\mathcal{H}_{\text{AL}} = V_0^* \Sigma_0 + V_0 \Sigma_0^{\dagger}, \tag{A2a}$$

$$\mathcal{L}_{\text{SE}}\rho = \Gamma\left(\frac{2J_e + 1}{2J_g + 1}\right) \sum_{q=-1}^{q=1} \mathcal{D}[\Sigma_q]\rho, \tag{A2b}$$

where $\mathcal{H}_{\text{AL}}$ and $\mathcal{L}_{\text{SE}}\rho$ are the Hamiltonian for the atom-laser interaction and spontaneous emission, respectively. The Rabi frequency for the coupling of the atoms in the ground state $F_g = 4$ and the excited state $F_e = 3$ with the laser is $V_0 = -\langle J_g \| d \| J_e \rangle E$, in which $\langle J_g \| d \| J_e \rangle$ and E are the electric-dipole matrix element and the laser amplitude, respectively. Symbols J_g and J_e are fine-structure angular momenta of the ground state and excited state. The lowering operator from Eqs. (A2a) and (A2b) between any two hyperfine structure

sublevels $|F_g, m_g\rangle$ and $|F_e, m_e\rangle$ is

$$
\begin{aligned}
\Sigma_q = \sum_{F_g, m_g F_e, m_e} & (-1)^{F_e + J_g + I + 1} C_{F_g m_g F_e m_e}^{1,q} \\
& \times \sqrt{(2F_e + 1)(2J_g + 1)} \\
& \times \begin{Bmatrix} J_e & J_g & 1 \\ F_g & F_e & I \end{Bmatrix} |F_g, m_g\rangle \langle F_e, m_e|,
\end{aligned} \tag{A3}
$$

where I is the nuclear spin quantum number and $\{:::\}$ is the Wigner 6-j symbol. The Lindblad superoperator $\mathcal{D}[\Sigma_q]\rho$ is defined by $\mathcal{D}[\Sigma_q]\rho = \Sigma_q \rho \Sigma_q^\dagger - \frac{1}{2}\Sigma_q^\dagger \Sigma_q \rho - \frac{1}{2}\rho \Sigma_q^\dagger \Sigma_q$. The subscript q takes $-1, 0, 1$ corresponding to the σ_- transition, π transition, and σ_+ transition, respectively. The coefficient Γ is the rate of spontaneous emission. Since the pumping rate V_0 of the linearly polarized pump-probe laser is much smaller than the decay rate Γ of the spontaneous emission, i.e., $V_0 \ll \Gamma$, the matrix elements $\rho_{F_e m, F_g m}$ between the ground state and the hyperfine sublevels of the excited state can be obtained by adiabatically removing the excited states $|F_e, m_e\rangle$ according to adiabatic approximation [81], where m means that the indices of the hyperfine sublevels of the ground and excited states are equal ($m_g = m_e$). The details of the density matrix elements $\rho_{F_e m, F_g m}$ are given by

$$
\rho_{F_g m F_e m} = \frac{8i\Lambda_{F_g m}^{F_e m} V_0}{3\Gamma} \rho_{F_g m F_g m}, \tag{A4}
$$

with

$$
\begin{aligned}
\Lambda_{F_g m}^{F_e m} = & (-1)^{m + J_g + I} \sqrt{2J_g + 1} \begin{pmatrix} F_e & 1 & F_g \\ m & q & -m \end{pmatrix} \\
& \times \sqrt{(2F_g + 1)(2F_e + 1)} \begin{Bmatrix} J_g & J_e & 1 \\ F_e & F_g & I \end{Bmatrix}.
\end{aligned} \tag{A5}
$$

The off-diagonal matrix element $\rho_{F_e m, F_g m}$ is related to the detection absorption of the linearly polarized pump-probe laser. Therefore, the linearly polarized pump-probe laser absorption

is [82–84]

$$
\alpha = \alpha_0 \sum_{m=-4}^{m=4} \frac{|\Lambda_{F_g m}^{F_e m} \langle J_g \| d \| J_e \rangle|^2}{\Lambda_{F_g m}^{F_e m} V_0} \operatorname{Im}[\rho_{F_g m F_g m}]. \tag{A6}
$$

Here the coefficient $\alpha_0 = 4\pi N \omega_L / \hbar c$ is a constant, where N is the atomic density, ω_L is the pump-probe laser transition frequency in the absence of a magnetic field, c is the speed of light, and $\hbar$ is Planck's constant. According to the transformation relationship $\rho_{F_g m F_g m} = \sum_{k=0}^{k=2F_g} \sum_{q=-k}^{q=k} (-1)^{F_g - m} \sqrt{2k+1} \begin{pmatrix} F_g & F_g & k \\ m & -m & -q \end{pmatrix} m_{k,q}^{\text{lab}}$ between the density matrix element and the state multipole $m_{k,q}^{\text{lab}}$ [49], the pump-probe laser absorption expression in the tensor representation is obtained as

$$
\alpha = \frac{\alpha_0}{9}\left(14 m_{0,0}^{\text{lab}} - \sqrt{77} m_{2,0}^{\text{lab}}\right), \tag{A7}
$$

where the atomic multipole moments $m_{0,0}^{\text{lab}}$ and $m_{2,0}^{\text{lab}}$ are the monopole moment and alignment in the laboratory frame [36], respectively. The alignment magnetic-resonance absorption spectra described by atomic multipole moments for the linearly polarized pump-probe laser is proportional to $C_0 m_{0,0}^{\text{lab}} + C_2 m_{2,0}^{\text{lab}}$. The coefficients C_0 and C_2 contain analyzing power, amplifier gain factors, and optical power dependencies [45]. The monopole moment $m_{0,0}^{\text{lab}}$ is related to the total population of ground-state atoms [76], which is just a number and has nothing to do with the information carried by the spectra. The main influence on the spectra is alignment $m_{2,0}^{\text{lab}}$. Therefore, the laser-detected alignment magnetic-resonance spectra can be given by

$$
S^{\text{lab}}(\omega_p) = C_2 m_{2,0}^{\text{lab}}. \tag{A8}
$$

APPENDIX B: DERIVATION OF EQS. (4) AND (6)

The total Hamiltonian in the dressed-state representation with rotating frequency Ω is

$$
H'_{\text{tot}}(t) = H'_2(t) + H'_p(t), \tag{B1}
$$

with

$$
\begin{aligned}
H'_2(t) = & \Omega_2\left(\cos^2\frac{\beta}{2} F'_{-1} e^{-i\Omega t} + \sqrt{2}\cos\frac{\beta}{2}\sin\frac{\beta}{2} F'_0 + \sin^2\frac{\beta}{2} F'_1 e^{i\Omega t}\right) e^{i\delta t} \\
& - \Omega_2\left(\sin^2\frac{\beta}{2} F'_{-1} e^{-i\Omega t} - \sqrt{2}\cos\frac{\beta}{2}\sin\frac{\beta}{2} F'_0 + \cos^2\frac{\beta}{2} F'_1 e^{i\Omega t}\right) e^{-i\delta t},
\end{aligned} \tag{B2a}
$$

$$
\begin{aligned}
H'_p(t) = & \Omega_p\left(\cos^2\frac{\beta}{2} F'_{-1} e^{-i\Omega t} + \sqrt{2}\cos\frac{\beta}{2}\sin\frac{\beta}{2} F'_0 + \sin^2\frac{\beta}{2} F'_1 e^{i\Omega t}\right) e^{i\delta_p t} \\
& - \Omega_p\left(\sin^2\frac{\beta}{2} F'_{-1} e^{-i\Omega t} - \sqrt{2}\cos\frac{\beta}{2}\sin\frac{\beta}{2} F'_0 + \cos^2\frac{\beta}{2} F'_1 e^{i\Omega t}\right) e^{-i\delta_p t},
\end{aligned} \tag{B2b}
$$

where the Hamiltonian $H'_2(t)$ and $H'_p(t)$ are derived from the Hamiltonian H_2 and H_p in the original representation, respectively. In the Hamiltonian H'_2, the terms containing F'_0 directly synthesize the longitudinal first harmonic Floquet

modulation

$$
{}^{1\text{st}}H_{\text{tot}}^{\text{eff}}(t) = 2\sqrt{2}\Omega_2 \cos\frac{\beta}{2}\sin\frac{\beta}{2} F'_0 \cos\delta t. \tag{B3}
$$

The high-frequency oscillation terms with frequencies $(\Omega \pm \delta)$ and $(\Omega \pm \delta_p)$ in the Hamiltonian $H'_{\text{tot}}(t)$ satisfy the conditions $(\Omega \pm \delta)$, $(\Omega \pm \delta_p) \gg \cos^2 \frac{\beta}{2} \Omega_2$, $\sin^2 \frac{\beta}{2} \Omega_2$, $\cos^2 \frac{\beta}{2} \Omega_p$, $\sin^2 \frac{\beta}{2} \Omega_p$, so these terms can use the perturbation theory [50,85] to give the effective Hamiltonian. For the effective Hamiltonian of each order, the low-frequency terms are kept and the high-frequency oscillation terms are ignored. Therefore, the effective Hamiltonian is given by

$$H_{\text{tot}}^{\text{eff}}(t) = {}^{\text{2nd}}H_{\text{tot}}^{\text{eff}}(t) + {}^{\text{3nd}}H_{\text{tot}}^{\text{eff}}(t), \tag{B4}$$

where the parameters ${}^{\text{2nd}}H_{\text{tot}}^{\text{eff}}$ and ${}^{\text{3rd}}H_{\text{tot}}^{\text{eff}}$ represent the second- and third-order effective Hamiltonians, respectively. The second-order effective Hamiltonian is given by

$$
\begin{aligned}
{}^{\text{2nd}}H_{\text{tot}}^{\text{eff}}(t) &= -iH'_{\text{tot}}(t) \int^t dt' H'_{\text{tot}}(t') \\
&= -i[H'_2(t) + H'_p(t)] \int^t dt'[H'_2(t') + H'_p(t')] \\
&= {}^{\text{2nd}}H_{22}^{\text{eff}}(t) + {}^{\text{2nd}}H_{2p}^{\text{eff}}(t) + {}^{\text{2nd}}H_{pp}^{\text{eff}}(t),
\end{aligned} \tag{B5}
$$

with

$$
\begin{aligned}
{}^{\text{2nd}}H_{22}^{\text{eff}} &= -iH'_2(t) \int^t dt' H'_2(t') \\
&\approx \omega_{\text{BS}} F'_0 - 2\cos^2 \frac{\beta}{2} \sin^2 \frac{\beta}{2} \frac{\Omega_2^2}{\Omega} F'_0 \cos 2\delta t,
\end{aligned} \tag{B6a}
$$

$$
\begin{aligned}
{}^{\text{2nd}}H_{2p}^{\text{eff}} &= -iH'_2(t) \int^t dt' H'_p(t') - iH'_p(t) \int^t dt' H'_2(t') \\
&\approx \Omega_p \left(\sqrt{2} \cos \frac{\beta}{2} \sin^3 \frac{\beta}{2} \frac{\Omega_2}{\Omega} e^{-i\delta t} - \sqrt{2} \sin \frac{\beta}{2} \cos^3 \frac{\beta}{2} \frac{\Omega_2}{\Omega} e^{i\delta t} \right) F'_{-1} e^{-i(\Omega+\delta_p)t} \\
&\quad - \Omega_p \left(\sqrt{2} \cos \frac{\beta}{2} \sin^3 \frac{\beta}{2} \frac{\Omega_2}{\Omega} e^{i\delta t} - \sqrt{2} \sin \frac{\beta}{2} \cos^3 \frac{\beta}{2} \frac{\Omega_2}{\Omega} e^{-i\delta t} \right) F'_1 e^{i(\Omega+\delta_p)t} \\
&\quad + \Omega_p \left(\sqrt{2} \cos \frac{\beta}{2} \sin^3 \frac{\beta}{2} \frac{\Omega_2}{\Omega} e^{-i\delta t} - \sqrt{2} \sin \frac{\beta}{2} \cos^3 \frac{\beta}{2} \frac{\Omega_2}{\Omega} e^{i\delta t} \right) F'_{-1} e^{-i(\Omega-\delta_p)t} \\
&\quad - \Omega_p \left(\sqrt{2} \cos \frac{\beta}{2} \sin^3 \frac{\beta}{2} \frac{\Omega_2}{\Omega} e^{i\delta t} - \sqrt{2} \sin \frac{\beta}{2} \cos^3 \frac{\beta}{2} \frac{\Omega_2}{\Omega} e^{-i\delta t} \right) F'_1 e^{i(\Omega-\delta_p)t},
\end{aligned} \tag{B6b}
$$

$$
{}^{\text{2nd}}H_{pp}^{\text{eff}} = -iH'_p(t) \int^t dt' H'_p(t'). \tag{B6c}
$$

Here frequency shift $\omega_{\text{BS}} = \Omega_2^2 \left(\frac{\sin^4 \frac{\beta}{2}}{\Omega+\delta} + \frac{\cos^4 \frac{\beta}{2}}{\Omega-\delta} \right)$ is the Bloch-Siegert-like shift [8]. The effective Hamiltonian ${}^{\text{2nd}}H_{22}^{\text{eff}}(t)$ is the second-order modification of the weak rf field $B_2(t)$. The effective Hamiltonian ${}^{\text{2nd}}H_{2p}^{\text{eff}}(t)$ is the second-order modification of the weak rf field $B_2(t)$ and probe field $B_p(t)$.

The effective Hamiltonian ${}^{\text{2nd}}H_{pp}^{\text{eff}}(t)$ is the second-order self-modification of the probe field $B_p(t)$. Note that since the Rabi frequency Ω_p of the probe field is very small, the second-order effect ${}^{\text{2nd}}H_{pp}^{\text{eff}}(t)$ can be ignored. The third-order effective Hamiltonian is

$$
\begin{aligned}
{}^{\text{3nd}}H_{\text{tot}}^{\text{eff}}(t) &= -H'_{\text{tot}}(t) \int^t H'_{\text{tot}}(t') \int^{t'} H'_{\text{tot}}(t'')dt''dt' \\
&= -[H'_2(t) + H'_p(t)] \int^t [H'_2(t') + H'_p(t')] \int^{t'} [H'_2(t'') + H'_p(t'')]dt''dt' \\
&= {}^{\text{3rd}}H_{22}^{\text{eff}}(t) + {}^{\text{3rd}}H_{2p}^{\text{eff}}(t) + {}^{\text{3rd}}H_{pp}^{\text{eff}}(t),
\end{aligned} \tag{B7}
$$

with

$$
\begin{aligned}
{}^{\text{3rd}}H_{22}^{\text{eff}}(t) &= -H'_2(t) \int^t H'_2(t') \int^{t'} H'_2(t'')dt''dt' \\
&\approx 2\sqrt{2}\Omega_2^3 \left(\frac{\cos^5 \frac{\beta}{2} \sin \frac{\beta}{2}}{2\delta\Omega - \Omega^2} - \frac{\cos \frac{\beta}{2} \sin^5 \frac{\beta}{2}}{2\delta\Omega + \Omega^2} - \frac{\cos^3 \frac{\beta}{2} \sin^3 \frac{\beta}{2}}{\delta^2 - \Omega^2} \right) F'_0 \cos \delta t \\
&\quad + \frac{2\sqrt{2}\Omega_2^3(2\delta^2 + \Omega^2)\cos^3 \frac{\beta}{2} \sin^3 \frac{\beta}{2}}{(4\delta^2 - \Omega^2)(\delta^2 - \Omega^2)} F'_0 \cos 3\delta t,
\end{aligned} \tag{B8a}
$$

$$^{3\mathrm{rd}}H_{2p}^{\mathrm{eff}}(t) = -\big[H_2'(t) + H_p'(t)\big]\bigg[\int^t H_2'(t') \int^{t'} H_p'(t'')dt''dt' + \int^t H_p'(t') \int^{t'} H_2'(t'')dt''dt'\bigg]$$
$$- H_2'(t)\int^t H_p'(t') \int^{t'} H_p'(t'')dt''dt' - H_p'(t)\int^t H_2'(t') \int^{t'} H_2'(t'')dt''dt', \tag{B8b}$$

$$^{3\mathrm{rd}}H_{pp}^{\mathrm{eff}}(t) = -H_p'(t)\int^t H_p'(t') \int^{t'} H_p'(t'')dt''dt'. \tag{B8c}$$

The effective Hamiltonians $^{3\mathrm{rd}}H_{22}^{\mathrm{eff}}(t)$, $^{3\mathrm{rd}}H_{2p}^{\mathrm{eff}}(t)$, and $^{3\mathrm{rd}}H_{pp}^{\mathrm{eff}}(t)$ represent the third-order self-modification of the weak rf field $B_2(t)$, the third-order modification between the weak rf field $B_2(t)$ and the probe field $B_p(t)$, and the third-order self-modification of the probe field $B_p(t)$, respectively. In our experiments, typical values of the optimized experimental parameters are $\omega_0 \approx$ 152.210 kHz, $\omega_1 \approx$ 152.210 kHz, $\omega_2 \approx$ 152.220 kHz, $\Omega_1 \approx$ 810 Hz, $\Omega_2 \approx$ 243Hz, $\Gamma \approx$ 50 Hz, and $\Omega_p \approx$ 20 Hz. Combined with our experimental parameters and the comprehensive analysis of Eqs. (B3) and (B8a), the first harmonic coefficient in Eq. (B3) is much larger than that in Eq. (B8a), so the first harmonic modulation generated by the third-order perturbation can be ignored. The coefficient of the second harmonic in Eq. (B6a) is much larger than the coefficient of the third harmonic in Eq. (B8a), so the third harmonic modulation present in the system can be ignored. Considering that Ω_p is much smaller than Ω_2, the Hamiltonian $^{3\mathrm{rd}}H_{2p}^{\mathrm{eff}}(t)$ and $^{3\mathrm{rd}}H_{pp}^{\mathrm{eff}}(t)$ in the third-order effective Hamiltonian $^{3\mathrm{rd}}H_{\mathrm{tot}}^{\mathrm{eff}}(t)$ can also be ignored. Therefore, the total Hamiltonian with the second-order modification effect is given by

$$H'(t) = \Omega_2 m(t)F_0' + \Omega_p[f_\pm(t)F_{-1}'e^{-i\delta_\pm t} - f_\pm^*(t)F_1'e^{i\delta_\pm t}], \tag{B9}$$

with

$$m(t) = 2\sqrt{2}\cos\frac{\beta}{2}\sin\frac{\beta}{2}\cos\delta t - 2\frac{\Omega_2}{\Omega}\cos^2\frac{\beta}{2}\sin^2\frac{\beta}{2}\cos 2\delta t, \tag{B10a}$$

$$f_\pm(t) = \frac{1 \pm \cos\beta}{2} + \sqrt{2}\frac{\Omega_2}{\Omega+\delta}\cos\frac{\beta}{2}\sin^3\frac{\beta}{2}e^{-i\delta t} - \sqrt{2}\frac{\Omega_2}{\Omega-\delta}\cos^3\frac{\beta}{2}\sin\frac{\beta}{2}e^{i\delta t}, \tag{B10b}$$

where the detuning $\delta_\pm$ is given by $\delta_\pm = \Omega + \omega_{\mathrm{BS}} \mp \delta_p$. The subscript "+" ("−") corresponds to the right (left) sideband of the spectra. The dimensionless parameters $m(t)$ and $f_\pm(t)$ are related to the Floquet modulation and probe modification, respectively. Next, the Floquet transformation is performed on the Hamiltonian, and the transformation operator $U(t)$ is

$$U(t) = e^{-i\int^t dt'\Omega_2 m(t')F_0'} = e^{-i(\xi_1\sin\delta t - \xi_2\sin 2\delta t)F_0'}, \tag{B11}$$

where the dimensionless parameters ξ_1 and ξ_2 are $\xi_1 = 2\sqrt{2}\cos\frac{\beta}{2}\sin\frac{\beta}{2}\frac{\Omega_2}{\delta}$ and $\xi_2 = \cos^2\frac{\beta}{2}\sin^2\frac{\beta}{2}\frac{\Omega_2^2}{\Omega\delta}$, respectively. The Hamiltonian $H'(t)$ after Floquet transformation $U(t)$ is

$$H_F'(t) = U^\dagger(t)H'(t)U(t) + i\frac{dU^\dagger(t)}{dt}U(t)$$
$$= \Omega_p \sum_{l=-\infty}^{l=+\infty}\sum_{n=-\infty}^{n=+\infty} J_{2n+l}(\xi_1)J_n(\xi_2)f_\pm(t)F_{-1}'e^{-i(\delta_\pm+l\delta)t}$$
$$- \Omega_p \sum_{l=-\infty}^{l=+\infty}\sum_{n=-\infty}^{n=+\infty} J_{2n+l}(\xi_1)J_n(\xi_2)f_\pm^*(t)F_1'e^{i(\delta_\pm+l\delta)t}. \tag{B12}$$

Here the identity relationship $e^{ix\sin\theta} = \sum_{m=-\infty}^{m=+\infty} e^{im\theta}J_m(x)$ is used, which can be obtained by the Laurent series expansion of the function $e^{\frac{1}{2}x(t-\frac{1}{t})}$ in $0 < |t| < \infty$ and taking $t = e^{i\theta}$ (x is the parameter variable) [53]. Therefore, the lth Floquet Hamiltonian with rotating frequency $l\delta$ is given by

$$H_F'^{(l)} = \Delta_\pm F_0' + \Omega_\pm^{(l)}(F_{-1}' - F_1'), \tag{B13}$$

with

$$\Omega_\pm^{(l)} = \frac{1 \pm \cos\beta}{2}\Omega_p \sum_{n=-\infty}^{n=+\infty} J_{2n+l}(\xi_1)J_n(\xi_2)$$
$$- \cos^3\frac{\beta}{2}\sin\frac{\beta}{2}\frac{\sqrt{2}\Omega_2\Omega_p}{\Omega-\delta} \sum_{n=-\infty}^{n=+\infty} J_{2n+l+1}(\xi_1)J_n(\xi_2)$$
$$+ \cos\frac{\beta}{2}\sin^3\frac{\beta}{2}\frac{\sqrt{2}\Omega_2\Omega_p}{\Omega+\delta} \sum_{n=-\infty}^{n=+\infty} J_{2n+l-1}(\xi_1)J_n(\xi_2), \tag{B14}$$

where the probe Rabi frequency $\Omega_\pm^{(l)}$ is the modified Rabi frequency with nonlinearity. The detuning $\Delta_\pm$ is defined by $\Delta_\pm = \delta_\pm + l\delta$. The evolution of the density matrix is governed by the master equation

$$\dot\rho = -i\big[H_F'^{(l)}, \rho\big] + L\rho, \tag{B15}$$

where $L\rho$ represents the relaxation process of the system, which is mainly composed of three types of relaxation processes: the optical pump relaxation process [86], the ground-state spin-exchange collision relaxation process [87,88], and the transit relaxation process [44]. To study the evolution of alignment concisely, we expand the density operator ρ into an ensemble of polarized atoms with hyperfine angular momentum according to the atomic multipole moments $m_{k,q}$:

$$\rho = \sum_{k=0}^{2F}\sum_{q=-k}^{k} m_{k,q}T_{k,q}, \tag{B16}$$

where $T_{k,q}$ is the irreducible tensor [49]. The multipole moments $m_{k,q}$ are defined by $m_{k,q} = \langle T_{k,q}^\dagger \rangle = tr\rho T_{k,q}^\dagger$ [36]. According to Eqs. (B13), (B15), and (B16), the evolution of the alignment components $m_{2,q}^{(l)}$ of the atomic ensemble is

$$\dot{m}_{2,-2}^{(l)} = i2\Delta_\pm^{(l)} m_{2,-2}^{(l)} - i\sqrt{2}\Omega_\pm^{(l)} m_{2,-1}^{(l)} - \Gamma_{2,-2} m_{2,-2}^{(l)}, \tag{B17a}$$

$$\dot{m}_{2,-1}^{(l)} = i\Delta_\pm^{(l)} m_{2,-1}^{(l)} - i\sqrt{3}\Omega_\pm^{(l)} m_{2,0}^{(l)} - i\sqrt{2}\Omega_\pm^{(l)} m_{2,-2}^{(l)} - \Gamma_{2,-1} m_{2,-1}^{(l)}, \tag{B17b}$$

$$\dot{m}_{2,0}^{(l)} = -i\sqrt{3}\Omega_\pm^{(l)} m_{2,-1}^{(l)} - i\sqrt{3}\Omega_\pm^{(l)} m_{2,1}^{(l)} - \Gamma_{2,0} m_{2,0}^{(l)} - \Gamma_{0,0} m_{0,0}, \tag{B17c}$$

$$\dot{m}_{2,1}^{(l)} = -i\Delta_\pm^{(l)} m_{2,1}^{(l)} - i\sqrt{3}\Omega_\pm^{(l)} m_{2,0}^{(l)} - i\sqrt{2}\Omega_\pm^{(l)} m_{2,2}^{(l)} - \Gamma_{2,1} m_{2,1}^{(l)}, \tag{B17d}$$

$$\dot{m}_{2,2}^{(l)} = -i2\Delta_\pm^{(l)} m_{2,2}^{(l)} - i\sqrt{2}\Omega_\pm^{(l)} m_{2,1}^{(l)} - \Gamma_{2,2} m_{2,2}^{(l)}, \tag{B17e}$$

where the coefficient $\Gamma_{2,q}$ (with $q = -2, \ldots, 2$) is the relaxation coefficient of alignment and satisfies the relationship $\Gamma_{2,q} = \Gamma_{2,|q|}$ [46]. The monopole moment $m_{0,0}$ is the injection of the system, which is equal to the population divided by $\sqrt{2F+1}$ [76]. When the steady-state condition $\partial_t m_{2,0}^{(l)} \equiv 0$ is satisfied, the solution of the incoherent component of the lth alignment is

$$\frac{m_{2,0}^{(l)}}{m_{0,0}} = \frac{\Gamma_{0,0}\left[\left(\Delta_\pm^{(l)2} + \Gamma_{2,1}^2\right)\left(4\Delta_\pm^{(l)2} + \Gamma_{2,2}^2\right) - 4\left(2\Delta_\pm^{(l)2} + \Gamma_{2,1}\Gamma_{2,2}\right)\left|\Omega_\pm^{(l)}\right|^2 + 4\left|\Omega_\pm^{(l)}\right|^4\right]}{(-)Z}, \tag{B18}$$

with

$$Z = 4(\Gamma_{2,0} + 3\Gamma_{2,2})\left|\Omega_\pm^{(l)}\right|^4 + \Gamma_{2,0}\left(\Delta_\pm^{(l)2} + \Gamma_{2,1}^2\right)\left(4\Delta_\pm^{(l)2} + \Gamma_{2,2}^2\right)$$
$$+ 2\left[\Gamma_{2,1}\Gamma_{2,2}(2\Gamma_{2,0} + 3\Gamma_{2,2}) - 4\Delta_\pm^{(l)2}(\Gamma_{2,0} - 3\Gamma_{2,1})\right]\left|\Omega_\pm^{(l)}\right|^2. \tag{B19}$$

Equation (B18) can be simplified substantially if we consider the isotropic relaxation process, i.e., $\Gamma_{2,2} \simeq \Gamma_{2,1} \simeq \Gamma_{2,0} \equiv \Gamma$, which is without loss of generality. The steady-state analytical expression of alignment $m_{2,0}^{(l)}$ is given by

$$m_{2,0}^{(l)} = \frac{1}{3} - \frac{1}{4}\left[\frac{\left|\Omega_\pm^{(l)}\right|^2}{\Delta_\pm^{(l)2} + \gamma_{1\pm}^2} - \frac{3\left|\Omega_\pm^{(l)}\right|^4}{4^2\left(\Delta_\pm^{(l)2} + \gamma_{1\pm}^2\right)\left(\Delta_\pm^{(l)2} + \gamma_{2\pm}^2\right)}\right], \tag{B20}$$

where the spectral linewidths $\gamma_{1\pm}^2 = \Gamma^2 + |\Omega_\pm^{(l)}|^2/4$ and $\gamma_{2\pm}^2 = (\Gamma^2 + |\Omega_\pm^{(l)}|^2)/4$. The symbol "+"("−") corresponds to the right (left) sideband for the incoherent term of alignment of the lth Floquet state. The first term of Eq. (B20) is constant, which has nothing to do with the information carried by the spectra and can be ignored. The second term is the standard Lorentz line type. The third term is formed by the multiplication of two Lorentz spectra with different line widths, which is the correction term of the spectra. The spectra (6) is obtained by substituting Eq. (B20) into Eq. (1).

APPENDIX C: CHARACTERISTICS FOR THE SQUARE OF THE ABSOLUTE VALUE OF THE PROBE RABI FREQUENCY $|\Omega_\pm^{(l)}|^2$

According to Eq. (B20), with the weak probe power limit ($\Omega_p \to 0$), the alignment magnetic-resonance spectra can be considered to be formed by the superposition of infinite Lorentz peaks with different resonance positions $\omega_1 \pm (\Omega + \omega_{BS} + l\delta)$. The peak value of each Lorentz peak is proportional to $|\Omega_\pm^{(l)}|^2$ and the contribution of Lorentz peaks at different resonance positions to the alignment magnetic-resonance spectra is different. Moreover, according to Figs. 8(a) to 8(f), the distribution of $|\Omega_\pm^{(l)}|^2$ with the Floquet summation index l is similar to the distribution of the alignment magnetic resonance spectra with the probe frequency ω_p. Therefore, studying the characteristics of $|\Omega_\pm^{(l)}|^2$ is helpful to understand the properties of the alignment magnetic reso-

nance spectra. According to Eq. (B14) and Figs. 8(a) to 8(f), the following conclusions are drawn.

(i) When only the first harmonic modulation is considered ($\xi_2 = 0$), $|\Omega_+^{(l)}|^2$ is symmetric about $l = 0$; when both the first harmonic and the second harmonic modulation are considered, $|\Omega_+^{(l)}|^2$ is asymmetric about $l = 0$ and the positions of the maxima and submaxima will shift.

(ii) When only the first harmonic modulation is considered, the position P_{right} of the maximum value on the right of $|\Omega_+^{(l)}|^2$ and the position P_{left} of the maximum value on the left and the argument ξ_1 approximately satisfy the relationship respectively: $P_{\text{right}} = [\xi_1] - k$ and $P_{\text{left}} = -|[\xi_1] + k|$, ($k = 0, 1, 2, \ldots,$), where $[x]$ denotes the integer part satisfying the relation $[x] \leqslant x < [x] + 1$. The value range of the variable ξ_1 is different and the corresponding value of k is also different. As shown in Fig. 8(a), when the value of ξ_1 is small, the value of k is approximately considered to be zero. When the value of ξ_1 is larger, the value of k is nonzero [see Figs. 8(b) and 8(c)].

(iii) As shown in Figs. 8(e) and 8(f), when ξ_1 is large, the position $\mathcal{P}_{\text{left}}$ of the submaximum of $|\Omega_+^{(l)}|^2$ is offset compared to the position P_{left} in conclusion (ii). The position of the submaximum can be expressed as $\mathcal{P}_{\text{left}} = -|[\xi_1] + k_1|$, ($k_1 = 0, 1, 2, \ldots,$). The position $\mathcal{P}_{\text{right}}$ of the maximum value of $|\Omega_+^{(l)}|^2$ is also offset from the position P_{right} in conclusion (ii), which is $\mathcal{P}_{\text{right}} = [\xi_1] - k_2$, ($k_2 = 0, 1, 2, \ldots,$). It is especially worth noting that when Ω_2 is large, k_1 and k_2 are not equal. Therefore, the interval $\Delta\mathcal{P}$ between the maxima
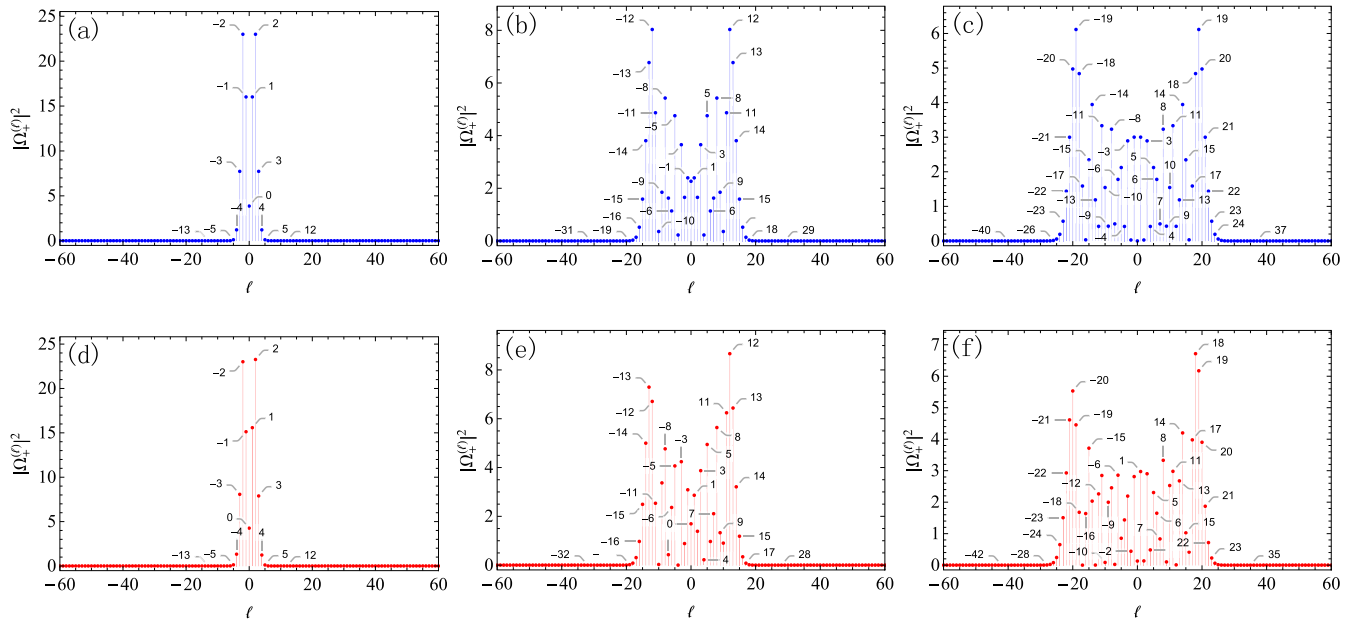
FIG. 8. The square of absolute value of probe Rabi frequency $\Omega_+^{(l)}$ versus the Floquet summation index l for right continuum. (a)–(c) consider only the first harmonic modulation ($2\sqrt{2}\Omega_2 \cos\frac{\beta}{2}\sin\frac{\beta}{2}\cos\delta t$). (d)–(f) are the cases where the first harmonic ($2\sqrt{2}\Omega_2 \cos\frac{\beta}{2}\sin\frac{\beta}{2}\cos\delta t$) and second harmonic ($-2\Omega_2\frac{\Omega_2}{\Omega}\cos^2\frac{\beta}{2}\sin^2\frac{\beta}{2}\cos 2\delta t$) modulation are considered at the same time. The parameters used in the calculation are (a) $\Omega_2 = 20$ Hz, $\xi_1 \approx 2.83$, $\xi_2 = 0$; (b) $\Omega_2 = 100$ Hz, $\xi_1 \approx 14.14$, $\xi_2 = 0$; (c) $\Omega_2 = 150$ Hz, $\xi_1 \approx 21.21$, $\xi_2 = 0$; (d) $\Omega_2 = 20$ Hz, $\xi_1 \approx 2.83$, $\xi_2 \approx 0.01$; (e) $\Omega_2 = 100$ Hz, $\xi_1 \approx 14.14$, $\xi_2 \approx 0.22$; (f) $\Omega_2 = 150$ Hz, $\xi_1 \approx 21.21$, $\xi_2 \approx 0.49$. Other parameters are $\omega_0 = 152.210$ kHz, $\omega_1 = 152.210$ kHz, $\Omega_1 = 810$ Hz, and $\Omega_p = 20$ Hz.

and submaxima is $\Delta\mathcal{P} = |\mathcal{P}_{\text{right}} - \mathcal{P}_{\text{left}}| = |2[\xi_1] + k_1 - k_2|$. Then in this case, when Ω_2 directly tends to 0, argument ξ_1 tends to 0, but $\Delta\mathcal{P}$ is $|k_1 - k_2| \neq 0$. However, by analyzing Fig. 8(d), when ξ_1 is small, the positions of the extreme values are basically consistent with conclusion (ii). However, in this case, the two extreme positions of the spectra are submerged within the linewidth and cannot be distinguished. Therefore, the position relationship of the extreme values of the spectra satisfied in the case of small Ω_2 and the case of large Ω_2 is different. In addition, the ratio of maxima to submaxima in the spectral continua can be approximately proportional to the ratio of the maxima to submaxima of $|\Omega_\pm^{(l)}|^2$.

(iv) Because the spectral continuum is synthesized by the summation of infinite Lorenz peaks with different resonance points, the average effect of the summation is also considered. Since the magnitude of the value of $|\Omega_+^{(l)}|^2$ corresponding to the different l on both sides of the extreme point of $|\Omega_+^{(l)}|^2$ is not symmetrical with respect to the extreme value position, the average effect of the summation will also shift the extreme value position of the continuum.

According to the above analysis of $|\Omega_\pm^{(l)}|^2$, the formation process and characteristics of the alignment magnetic-resonance spectra dressed by the double rf fields can be further understood.

[1] A. Eckardt, Rev. Mod. Phys. **89**, 011004 (2017).

[2] G. Y. Kryuchkyan, V. Shahnazaryan, O. V. Kibis, and I. A. Shelykh, Phys. Rev. A **95**, 013834 (2017).

[3] A. A. Pervishko, O. V. Kibis, S. Morina, and I. A. Shelykh, Phys. Rev. B **92**, 205403 (2015).

[4] M. Keunecke, M. Reutzel, D. Schmitt, A. Osterkorn, T. A. Mishra, C. Möller, W. Bennecke, G. S. Matthijs Jansen, D. Steil, S. R. Manmana, S. Steil, S. Kehrein, and S. Mathias, Phys. Rev. B **102**, 161403(R) (2020).

[5] T. Yabuzaki, S. Nakayama, Y. Murakami, and T. Ogawa, Phys. Rev. A **10**, 1955 (1974).

[6] N. Tsukada, T. Nakayama, S. Ibuki, T. Akiba, and K. Tomishima, Phys. Rev. A **23**, 1855 (1981).

[7] F. Bloch and A. Siegert, Phys. Rev. **57**, 522 (1940).

[8] A. P. Saiko, S. A. Markevich, and R. Fedaruk, Phys. Rev. A **98**, 043814 (2018).

[9] G. Bevilacqua, V. Biancalana, A. Vigilante, T. Zanon-Willette, and E. Arimondo, Phys. Rev. Lett. **125**, 093203 (2020).

[10] S. Haroche and C. Cohen-Tannoudji, Phys. Rev. Lett. **24**, 974 (1970).

[11] G. Bevilacqua, V. Biancalana, T. Zanon-Willette, and E. Arimondo, Phys. Rev. A **105**, 022619 (2022).

[12] C.-P. Hao, Z.-R. Qiu, Q. Sun, Y. Zhu, and D. Sheng, Phys. Rev. A **99**, 053417 (2019).

[13] V. Han and C. Liu, Magn. Reson. Med. **84**, 1184 (2020).

[14] L. I. Sacolick, F. Wiesinger, I. Hancu, and M. W. Vogel, Magn. Reson. Med. **63**, 1315 (2010).

[15] S. Bertaina, L. Chen, N. Groll, J. Van Tol, N. S. Dalal, and I. Chiorescu, Phys. Rev. Lett. **102**, 050501 (2009).

[16] J. P. Ashton and P. M. Lenahan, Phys. Rev. B **102**, 020101(R) (2020).

[17] M. Jing, Y. Hu, J. Ma, H. Zhang, L. Zhang, L. Xiao, and S. Jia, Nat. Phys. **16**, 911 (2020).

[18] Z. Liang, X. Geng, P. Qi, K. Jin, G. Yang, G. Li, and G. Huang, Opt. Express **29**, 33197 (2021).

[19] T. Hönigl-Decrinis, R. Shaikhaidarov, S. E. de Graaf, V. N. Antonov, and O. V. Astafiev, Phys. Rev. Applied **13**, 024066 (2020).

[20] G. Bao, A. Wickenbrock, S. Rochester, W. Zhang, and D. Budker, Phys. Rev. Lett. **120**, 033202 (2018).

[21] G. A. Sinuco-Leon, B. M. Garraway, H. Mas, S. Pandey, G. Vasilakis, V. Bolpasi, W. von Klitzing, B. Foxon, S. Jammi, K. Poulios, and T. Fernholz, Phys. Rev. A **100**, 053416 (2019).

[22] G. A. Sinuco-Leon, H. Mas, S. Pandey, G. Vasilakis, B. M. Garraway, and W. von Klitzing, Phys. Rev. A **104**, 033307 (2021).

[23] N. Y. Yao, C. R. Laumann, S. Gopalakrishnan, M. Knap, M. Müller, E. A. Demler, and M. D. Lukin, Phys. Rev. Lett. **113**, 243002 (2014).

[24] A. Kitaev, AIP Conf. Proc. **1134**, 22 (2009).

[25] J. Casado-Pascual, L. Lamata, and A. A. Reynoso, Phys. Rev. E **103**, 052139 (2021).

[26] A. A. Reynoso, J. P. Baltanás, H. Saarikoski, J. E. Vázquez-Lozano, J. Nitta, and D. Frustaglia, New J. Phys. **19**, 063010 (2017).

[27] A. Kyprianidis, F. Machado, W. Morong, P. Becker, K. S. Collins, D. V. Else, L. Feng, P. W. Hess, C. Nayak, G. Pagano, N. Y. Yao, and C. Monroe, Science **372**, 1192 (2021).

[28] P. Peng, C. Yin, X. Huang, C. Ramanathan, and P. Cappellaro, Nat. Phys. **17**, 444 (2021).

[29] Z. Shu, Y. Liu, Q. Cao, P. Yang, S. Zhang, M. B. Plenio, F. Jelezko, and J. Cai, Phys. Rev. Lett. **121**, 210501 (2018).

[30] M. L. Olivera-Atencio, J. Casado-Pascual, and S. Kohler, Eur. Phys. J. B **93**, 30 (2020).

[31] M. Jiang, H. Su, Z. Wu, X. Peng, and D. Budker, Sci. Adv. **7**, eabe0719 (2021).

[32] M. Jiang, Y. Qin, X. Wang, Y. Wang, H. Su, X. Peng, and D. Budker, Phys. Rev. Lett. **128**, 233201 (2022).

[33] D. Budker, P. W. Graham, M. Ledbetter, S. Rajendran, and A. O. Sushkov, Phys. Rev. X **4**, 021030 (2014).

[34] G. Wang, C. Li, and P. Cappellaro, Phys. Rev. Lett. **127**, 140604 (2021).

[35] G. Wang, Y.-X. Liu, J. M. Schloss, S. T. Alsid, D. A. Braje, and P. Cappellaro, Phys. Rev. X **12**, 021061 (2022).

[36] A. Weis, G. Bison, and A. S. Pazgalev, Phys. Rev. A **74**, 033401 (2006).

[37] T. Fernholz, H. Krauter, K. Jensen, J. F. Sherson, A. S. Sørensen, and E. S. Polzik, Phys. Rev. Lett. **101**, 073601 (2008).

[38] O. Katz, R. Shaham, E. S. Polzik, and O. Firstenberg, Phys. Rev. Lett. **124**, 043602 (2020).

[39] J. Kong, R. Jiménez-Martínez, C. Troullinou, V. G. Lucivero, G. Tóth, and M. W. Mitchell, Nat. Commun. **11**, 2415 (2020).

[40] D. Budker, W. Gawlik, D. F. Kimball, S. M. Rochester, V. V. Yashchuk, and A. Weis, Rev. Mod. Phys. **74**, 1153 (2002).

[41] S. M. Rochester, M. P. Ledbetter, T. Zigdon, A. D. Wilson-Gordon, and D. Budker, Phys. Rev. A **85**, 022125 (2012).

[42] S. J. Ingleby, C. O'Dwyer, P. F. Griffin, A. S. Arnold, and E. Riis, Phys. Rev. Applied **10**, 034035 (2018).

[43] F. Castellucci, T. W. Clark, A. Selyem, J. Wang, and S. Franke-Arnold, Phys. Rev. Lett. **127**, 233202 (2021).

[44] X. Geng, G. Yang, P. Qi, W. Tang, S. Liang, G. Li, and G. Huang, Phys. Rev. A **103**, 053112 (2021).

[45] G. Di Domenico, G. Bison, S. Groeger, P. Knowles, A. S. Pazgalev, M. Rebetez, H. Saudan, and A. Weis, Phys. Rev. A **74**, 063415 (2006).

[46] G. Bevilacqua, E. Breschi, and A. Weis, Phys. Rev. A **89**, 033406 (2014).

[47] R. Schmied, *Using Mathematica for Quantum Mechanics: A Student's Manual* (Springer Nature, Singapore, 2020).

[48] D. A. Varshalovich, A. N. Moskalev, and V. K. Khersonskii, *Quantum Theory of Angular Momentum* (World Scientific, Singapore, 1988).

[49] K. Blum, *Density Matrix Theory and Applications* (Springer, Boston, 1981).

[50] D. F. James and J. Jerke, Can. J. Phys. **85**, 625 (2007).

[51] L. Cao, J. Qi, J. Du, and J. Jing, Phys. Rev. A **95**, 023803 (2017).

[52] G. Li, H. Tan, and M. Macovei, Phys. Rev. A **76**, 053827 (2007).

[53] DLMF, NIST Digital Library of Mathematical Functions, http://dlmf.nist.gov/, Release 1.1.5 of 2022-03-15, edited by F. W. J. Olver, A. B. Olde Daalhuis, D. W. Lozier, B. I. Schneider, R. F. Boisvert, C. W. Clark, B. R. Miller, B. V. Saunders, H. S. Cohl, and M. A. McClain.

[54] Y. Yan, Z. Lü, J. Y. Luo, and H. Zheng, Phys. Rev. A **100**, 013823 (2019).

[55] B. Blind, P. R. Fontana, and P. Thomann, J. Phys. B **13**, 2717 (1980).

[56] D. M. Lukin, A. D. White, R. Trivedi, M. A. Guidry, N. Morioka, C. Babin, Ö. O. Soykal, J. Ul-Hassan, N. T. Son, T. Ohshima, P. K. Vasireddy, M. H. Nasr, S. Sun, J.-P. W. MacLean, C. Dory, E. A. Nanni, J. Wrachtrup, F. Kaiser, and J. Vučković, npj Quantum Inf. **6**, 80 (2020).

[57] F. Grossmann, T. Dittrich, P. Jung, and P. Hänggi, Phys. Rev. Lett. **67**, 516 (1991).

[58] E. Saglamyurek, T. Hrushevskyi, A. Rastogi, K. Heshami, and L. J. LeBlanc, Nat. Photonics **12**, 774 (2018).

[59] Y. He, Y.-M. He, J. Liu, Y.-J. Wei, H. Y. Ramírez, M. Atatüre, C. Schneider, M. Kamp, S. Höfling, C.-Y. Lu, and J.-W. Pan, Phys. Rev. Lett. **114**, 097402 (2015).

[60] M. O. Assunção, G. S. Diniz, L. Sanz, and F. M. Souza, Phys. Rev. B **98**, 075423 (2018).

[61] M. A. Sillanpää, J. Li, K. Cicak, F. Altomare, J. I. Park, R. W. Simmonds, G. S. Paraoanu, and P. J. Hakonen, Phys. Rev. Lett. **103**, 193601 (2009).

[62] H. S. Freedhoff and Z. Ficek, Phys. Rev. A **55**, 1234 (1997).

[63] I. M. Savukov, S. J. Seltzer, M. V. Romalis, and K. L. Sauer, Phys. Rev. Lett. **95**, 063004 (2005).

[64] V. Gerginov, Phys. Rev. Applied **11**, 024008 (2019).

[65] H. H. Jen and Y.-C. Chen, Phys. Rev. A **93**, 013811 (2016).

[66] M. C. Stowe, A. Pe'er, and J. Ye, Phys. Rev. Lett. **100**, 203001 (2008).

[67] M. Piccardo, M. Tamagnone, B. Schwarz, P. Chevalier, N. A. Rubin, Y. Wang, C. A. Wang, M. K. Connors, D. McNulty, A. Belyanin, and F. Capasso, Proc. Natl. Acad. Sci. **116**, 9181 (2019).

[68] Y. Yan, C. Liu, H. Wu, and Y. Dong, International Journal of Antennas and Propagation **2017**, 6198686 (2017).

[69] L. D. Turner, V. Karaganov, P. J. O. Teubner, and R. E. Scholten, Opt. Lett. **27**, 500 (2002).

[70] Z. He, Y. Zhang, H. Wu, P. Yuan, and S. Liu, J. Opt. Soc. Am. B **26**, 1755 (2009).

[71] J. Meinel, V. Vorobyov, B. Yavkin, D. Dasari, H. Sumiya, S. Onoda, J. Isoya, and J. Wrachtrup, Nat. Commun. **12**, 2737 (2021).

[72] R. Debroux, C. P. Michaels, C. M. Purser, N. Wan, M. E. Trusheim, J. Arjona Martínez, R. A. Parker, A. M. Stramma, K. C. Chen, L. de Santis, E. M. Alexeev, A. C. Ferrari, D. Englund, D. A. Gangloff, and M. Atatüre, Phys. Rev. X **11**, 041041 (2021).

[73] J. Wu, J. Liu, Y. He, Y. Zhang, J. Zhang, and S. Zhu, Phys. Rev. A **98**, 043829 (2018).

[74] I. M. Georgescu, S. Ashhab, and F. Nori, Rev. Mod. Phys. **86**, 153 (2014).

[75] G. Di Domenico, H. Saudan, G. Bison, P. Knowles, and A. Weis, Phys. Rev. A **76**, 023407 (2007).

[76] M. Auzinsh, D. Budker, and S. Rochester, *Optically Polarized Atoms: Understanding Light-Atom Interactions* (Oxford University Press, New York, 2010).

[77] P. Zhang, V. Kharchenko, A. Dalgarno, Y. Matsumi, T. Nakayama, and K. Takahashi, Phys. Rev. Lett. **100**, 103001 (2008).

[78] E. Breschi and A. Weis, Phys. Rev. A **86**, 053427 (2012).

[79] D. Loss and D. P. DiVincenzo, Phys. Rev. A **57**, 120 (1998).

[80] W. Happer, Rev. Mod. Phys. **44**, 169 (1972).

[81] Y. Chang, Y.-H. Guo, and J. Qin, Phys. Rev. A **99**, 063411 (2019).

[82] S. Menon and G. S. Agarwal, Phys. Rev. A **59**, 740 (1999).

[83] L. Margalit, M. Rosenbluh, and A. D. Wilson-Gordon, Phys. Rev. A **87**, 033808 (2013).

[84] T. Zigdon, A. D. Wilson-Gordon, and H. Friedmann, Phys. Rev. A **80**, 033825 (2009).

[85] R. Tan, G.-x. Li, and Z. Ficek, Phys. Rev. A **78**, 023833 (2008).

[86] P.-L. Qi, X. Geng, G. Yang, G. Huang, and G. Li, J. Opt. Soc. Am. B **37**, 3303 (2020).

[87] T. Scholtes, S. Pustelny, S. Fritzsche, V. Schultze, R. Stolz, and H.-G. Meyer, Phys. Rev. A **94**, 013403 (2016).

[88] Y. Shi, T. Scholtes, Z. D. Grujić, V. Lebedev, V. Dolgovskiy, and A. Weis, Phys. Rev. A **97**, 013419 (2018).